

Syracuse University

**SURFACE**

---

Dissertations - ALL

SURFACE

---

May 2019

## Composite Right-Left Handed Stripline Structures for Antenna Array Feed Networks

Michael Douglas Enders  
*Syracuse University*

Follow this and additional works at: <https://surface.syr.edu/etd>



Part of the [Engineering Commons](#)

---

### Recommended Citation

Enders, Michael Douglas, "Composite Right-Left Handed Stripline Structures for Antenna Array Feed Networks" (2019). *Dissertations - ALL*. 1031.

<https://surface.syr.edu/etd/1031>

This Dissertation is brought to you for free and open access by the SURFACE at SURFACE. It has been accepted for inclusion in Dissertations - ALL by an authorized administrator of SURFACE. For more information, please contact [surface@syr.edu](mailto:surface@syr.edu).

## ABSTRACT

In this dissertation composite right/left-handed striplines are proposed as viable key structures in antenna array applications, enabling reduction of the overall feed network sizes as well as allowing integration opportunities and possible reduction of radiating beam pattern distortions.

A via-less composite right/left-handed stripline unit cell is introduced as an option to attain right/left-handed performance in stripline with a via-less fabrication process that is not sensitive to drill positioning errors and is amenable to academic settings. An analysis of the passbands of this structure based on the distributed transmission line circuit theory is provided as well as a description of the method utilized to tune the performance.

Three different application scenarios are explored using variations of the via-less composite right/left-handed stripline in the feed networks. The first application is a linear frequency scanning antenna array in which arbitrary radiating elements may be used. The second application is in a 2D planar frequency scanning array that has the capability of steering radiated beams over most of a hemisphere. The last one is in a wideband phase shifting network that can be used to excite a circularly polarized antenna array. Comparisons to the traditional unit cell with vias are provided when appropriate, as well as comparisons to non composite right/left-handed approaches traditionally used for each application.

This practical research is supported by extensive 3D electromagnetic simulations and, for the via-less solutions, validated through scattering parameters and radiation pattern measurements of fabricated prototypes. The fabrication process is described in detail with emphasis on aspects that have the most significant effect on overall performance. The measured results presented are in good agreement with simulated predictions, bolstering the case for the use of composite right/left-handed striplines in antenna array feed networks.

**COMPOSITE RIGHT-LEFT HANDED STRIPLINE STRUCTURES FOR  
ANTENNA ARRAY FEED NETWORKS**

By

Michael D. Enders

B.S.E.E., Federal University of Rio Grande do Norte - Brazil, 2005  
M.S.E.E., Syracuse University, 2007

DISSERTATION

Submitted in partial fulfillment of the requirements for the degree of  
Doctor of Philosophy in Electrical and Computer Engineering.

Syracuse University

May 2019

Copyright © Michael D. Enders 2019

All Rights Reserved

“If you go back a few hundred years, what we take for granted today would seem like magic - being able to talk to people over long distances, to transmit images, flying, accessing vast amounts of data like an oracle. These are all things that would have been considered magic a few hundred years ago.”

*Elon R. Musk* - Founder of Space Exploration Technologies Corp. and Tesla Inc.

To my beloved daughters *Mia* and *Saskia*,  
to whom I wish to instill the curiosity to explore,  
the tenacity to persevere,  
the enthusiasm to cheer life,  
and, above all,  
the kindness the world needs.

## ACKNOWLEDGEMENTS

I would like to express my gratitude to my advisor Prof. Jay K. Lee, for his continued dedication to the Electrical Engineering undergraduate and graduate programs at the department and to the student body. I am also grateful to my co-advisor Prof. Jun H. Choi for guiding me through this journey these past few years and in particular for his understanding of the challenges associated with working on a doctoral program part time.

I would like to recognize the important role that Prof. Ercument Arvas has had for me to reach this point in my career and studies. He was involved in my selection to enroll at Syracuse University for the Masters of Science program, in connecting me to the local Syracuse area industry, and in my initial years in the doctoral program in which he was my advisor prior to retirement.

I am thankful to Prof. Jennifer W. Graham, Prof. Qi Wang Song and Prof. Mustafa C. Gursoy, for serving as Committee Members and dedicating time to review and comment on this dissertation. I am also grateful to Prof. Thong Q. Dang for participating as Chair of the Oral Examination Committee and representing the Graduate School.

I also thank the following Syracuse University entities: SU Computer Center, for providing computational resources; CASE Center, for providing PCB routing equipment; and Prof. M. M. Maye of the Chemistry Department for providing laboratory space for fabrication.

I'm also thankful to Anaren Inc., and JMA Wireless, which as employers have recognized the value of employees pursuing further education and supported my doctoral program in various ways.

A special acknowledgment is dedicated to my wife Chunhua who has taken on a lot these past several years in order to provide me with some free time from my responsibilities so that I could focus on exploring topics of research. Likewise, I would like to acknowledge my mother Bertha for always incentivising my pursuit of knowledge.

## TABLE OF CONTENTS

<b>Acknowledgments</b> . . . . .	vi
<b>List of Tables</b> . . . . .	x
<b>List of Figures</b> . . . . .	xi
<b>Chapter 1: Introduction</b> . . . . .	1
<b>Chapter 2: Fundamental Topics</b> . . . . .	3
2.1 Metamaterials . . . . .	3
2.2 Composite Right/Left-Handed Transmission Lines . . . . .	4
2.3 Frequency Scanning Antenna Arrays . . . . .	5
<b>Chapter 3: The Via-Less Composite Right/Left-Handed Stripline</b> . . . . .	8
3.1 Analysis of the Via-Less Composite Right/Left-Handed Transmission Line . . . . .	9
3.2 Passbands Determination . . . . .	17
3.3 Design Procedure . . . . .	18
<b>Chapter 4: Feed Networks for Linear Frequency Scanning Antenna Arrays</b> . . . . .	20
4.1 Feed Network Using Via-Less CRLH Stripline Unit Cell . . . . .	21
4.1.1 Unit Cell . . . . .	21
4.1.2 Series Feed . . . . .	23

4.2	Prototype . . . . .	26
4.2.1	Design . . . . .	26
4.2.2	Measurements Results . . . . .	26
4.3	Summary . . . . .	29
<b>Chapter 5: Feed Networks for 2D Frequency Scanning Antenna Arrays . . . . .</b>		<b>30</b>
5.1	Design . . . . .	31
5.1.1	Feed Network Using Via-Less CRLH Stripline Unit Cell . . . . .	32
5.1.2	Linear Antenna Arrays . . . . .	39
5.2	Measurements of an Integrated Array . . . . .	42
5.3	Radar Application Test . . . . .	47
5.4	Traditional CRLH Stripline Implementation . . . . .	51
5.5	Summary . . . . .	54
<b>Chapter 6: Wideband Phase Shifter Element . . . . .</b>		<b>56</b>
6.1	The Via-Less CRLH Stripline Unit Cell . . . . .	59
6.2	Traditional CRLH Stripline Unit Cell . . . . .	61
6.3	Summary . . . . .	64
<b>Chapter 7: Methodology . . . . .</b>		<b>67</b>
<b>Chapter 8: Manufacturing Considerations . . . . .</b>		<b>70</b>
8.1	Embedding Resistors . . . . .	70
8.2	Mechanical Etching and Drilling . . . . .	72
8.3	Chemical Wet Etching . . . . .	74

8.4 Mask Fidelity . . . . .	76
<b>Chapter 9: Conclusions . . . . .</b>	<b>78</b>
<b>Appendix A: Matlab Code: Via-Less CRLH TL Passbands Calculator . . . . .</b>	<b>81</b>
<b>References . . . . .</b>	<b>89</b>
<b>Vita . . . . .</b>	<b>90</b>

## LIST OF TABLES

5.1	Integrated Array Radiation Characteristics . . . . .	46
5.2	Radar Target Positions . . . . .	49

## LIST OF FIGURES

2.1	Materials characterized by permittivity and permeability. . . . .	3
2.2	a) CRLH unit cell; b) Dispersion diagram. . . . .	5
2.3	Example of microstrip implementation of a CRLH TL including interdigital capacitor and via. . . . .	5
2.4	Illustration of frequency scanning antenna array with series feed network where $k_0$ is the wave number in free space, $d$ is the distance between antennas, $s$ is the length of transmission line between antennas, and $\theta_m$ is the direction of far field beam peak off of broadside. . . . .	6
3.1	Via-less CRLH unit cell. (a) Top view of unit cell in modeler. (b) Schematic of unit cell. . . . .	8
3.2	Schematic of via-less CRLH unit cell as part of infinitely long periodic transmission line. . . . .	9
4.1	Stripline CRLH unit cell with stub to open patch. (a) Stripline stackup. (b) Fl = 355 mils, Fw = 10 mils, Sw = 20 mils, Sl = 110 mils, Pw = 110 mils and all gaps = 10 mils. (c) 3D EM simulated dispersion curve. . . . .	21
4.2	Linear FSA general schematic for equal power excitation at 4 ports. . . . .	23
4.3	Models of preliminary CRLH TL directional couplers. (a) Traditional model with 4-ports. (b) Performance of 4-port model with low directivity. (c) Model with 3-ports in which the directivity port is left as an open circuit. (d) Performance of the 3-port model indicates that the open circuit does not significantly affect the parameters of interest. . . . .	24

4.4	Models of preliminary CRLH stripline feed networks with different paths for last port. (a) Model with Port4 immediately after last directional coupler. (b) Phase progression of model in (a). (c) Model with extra CRLH unit cell on Port4 path. (d) Phase progression of model in (c). . . . .	25
4.5	Stripline CRLH feed network model. . . . .	26
4.6	Simulation results of model in Fig. 4.5. (a) Input return loss. (b) Output power. (c) Progressive phase offset of output ports - Port x relative to port y defined as $\text{angle}(S(x,\text{Input})/S(y,\text{Input}))$ . . . . .	27
4.7	Stripline prototype. (a) Bottom substrate prior to lamination. (b) Feeding antenna array in measurement setup. . . . .	27
4.8	Measured results from prototype in Fig. 4.7. (a) Input return loss. (b) Output power. (c) Progressive phase offset of output ports. (d) Radiation pattern of select frequencies (s at $\theta = 0^\circ$ ). . . . .	28
5.1	Diagram of the proposed 2D Frequency Scanning Array. . . . .	31
5.2	Phase progression relationship between directions. The feed network is in the primary direction and the linear arrays are in the secondary direction. . .	32
5.3	Compact (folded) via-less stripline unit cell used for feed network. (a) Stackup. (b) Geometry. (c) Dispersion. Length $l = 2.54$ mm. . . . .	34
5.4	Electric fields on a vertical cross section of a stripline in this stackup. (a) Full stripline model. (b) Stripline model using a perfect H boundary condition along the vertical center. . . . .	35
5.5	Top view of full feed network model in which perfect H boundary condition was used. . . . .	36
5.6	Feed network bottom board prior to lamination. . . . .	36
5.7	Via-less CRLH stripline versus traditional stripline area comparison. . . . .	37
5.8	Feed network test board. (a) Test board. (b) Return loss performance. (c) Output power. (d) Output phase progression. . . . .	38
5.9	Via-less CRLH loaded microstrip line unit cell used for LWA. (a) Stackup. (b) Geometry. (c) Dispersion and leakage constant. Length $l = 9$ mm. . . . .	40
5.10	Leaky wave antenna bottom board prior to lamination. . . . .	40

5.11	Leaky wave antenna test board. (a) Test board. (b) Return loss performance. (c) Scanning angle of leaky wave antenna. . . . .	42
5.12	Integrated prototype. (a) Bottom board. (b) Prototype. . . . .	43
5.13	Top view of full antenna array model. . . . .	44
5.14	Measurement results of the integrated prototype. (a) Return loss performance. (b) Sample of measured radiation patterns (normalized). (c) Scanning route (beam peak position as frequency is swept). . . . .	45
5.15	Radar application measurement results. Target detection within 5° cone of intended position. (a) Measurement setup for target detection. (b) Detected signals. (c) Target at position #1. (d) Target at position #2. (e) Target at position #3. . . . .	48
5.16	Traditional CRLH stripline unit cell in the same stackup tuned for balanced frequency of 6 GHz. (a) Top view of 3D Model. (b) Dispersion diagram. . . . .	52
5.17	Six traditional CRLH stripline unit cells cascaded. (a) Top view of 3D Model. (b) Phase progression of cascaded model. . . . .	53
6.1	Feed network for wideband circularly polarized antenna using lumped element CRLH TL for phase shifting. . . . .	57
6.2	Some examples of existent phase shifter options. (a) Various non-CRLH phase shifter options. (b) Example of CRLH microstrip phase shifter. . . . .	58
6.3	180° Phase Shifter with via-less unit cell. (a) 3D model of the 180° Phase Shifter, (b) Stripline stackup for broadside coupling, (c) Return Loss for 180° Phase Shifter, and (d) Phase shift offset to regular stripline. . . . .	60
6.4	90° Phase Shifter with traditional CRLH stripline unit cell. (a) 3D model. (b) Return Loss (c) Phase shift offset to regular stripline. . . . .	62
6.5	180° Phase Shifter with traditional CRLH stripline unit cell. (a) 3D model. (b) Return Loss (c) Phase shift offset to regular stripline. . . . .	63
6.6	4-Way splitting feed network with phase offsets (0°, 90°, 180°, and 270°) at 10 GHz. (a) Schematic, (b) Insertion phase, and (c) Wide band constant offset phase error. . . . .	65

6.7	4-Way splitting feed network with phase offsets ( $0^\circ$ , $90^\circ$ , $180^\circ$ , and $270^\circ$ ) at 10 GHz and with the traditional CRLH stripline phase shifters designed. (a) Schematic, (b) Insertion phase with better tracking over frequency, and (c) Wide band constant offset phase error significantly reduced. . . . .	66
8.1	Cavities for embedded resistors. (a) 3D Model. (b) Drill test to determine proper depth setting. . . . .	71
8.2	Example of cavities for resistors. Superstrate that mates with substrate in Fig. 5.6. . . . .	71
8.3	Simplified illustration of odd mode electric fields of edge coupled lines in: (a) microstrip with perfect etching (as commonly modeled). (b) microstrip with over milling. (c) stripline with perfect etching (as commonly modeled) (c) stripline with over milling. $\epsilon_{air} < \epsilon_{substrate}$ and $\epsilon_{bond} \approx \epsilon_{substrate} = \epsilon_{superstrate}$ . . . . .	73
8.4	Zoomed in views of the folded via-less CRLH stripline from an iteration of the substrate in Fig. 5.6. (a) LPKF camera capture. (b) Same image with auxiliary tool lines implemented in CAD software to determine distances. . . . .	75
8.5	Example of ruby mask. Ruby mask for artwork of substrate in Fig. 5.6. . . . .	76
8.6	Zoomed in views of ruby masks for artwork used in same network as Fig. 5.10. (a) Example of section with arc in drawing deforming linewidths of nearby sections. (b) Another example of arc causing deformation. (c) Example of arc of same location as in (a), replaced with segment approximation not introducing deformation. . . . .	77

# CHAPTER 1

## INTRODUCTION

The topic that is discussed in this dissertation is that of the advantages of the use of composite right/left-handed (CRLH) striplines as an integral part of feed networks in planar antenna array applications.

Stripline is a wave guiding technology that has been in existence for about as long as the ubiquitous microstrip [1] [2] and has become common in beam-forming networks in satellite [3] and radar applications. It has inherent shielding that makes it less susceptible to interference and reduces leakage radiation.

CRLH transmission lines (TLs) are structures capable of guiding electromagnetic (EM) waves with artificial wave propagation characteristics when considering amplitude and, of particular interest, phase. These artificial properties are akin to that of the general class of materials the scientific community has labeled *metamaterials*. These terms, along with the concept of a frequency scanning antenna array (FSAA), are explained in more detail in the next chapter (Chapter 2 - Fundamental Topics). Various implementations of CRLH TLs have been demonstrated including with lumped circuit elements [4], microstrip technology [5], substrate integrated waveguide (SIW) [6], cylindrical waveguides [7], and even more complex structures such as the folded SIW [8].

The CRLH TLs are capable of providing multiband and broadband functionality, and are often explored due to the opportunity to provide solutions with reduced overall package sizes. They are able to shrink the sizes of typical microwave circuit features such as power dividers [9], branch-line couplers [10] and antennas [11]. A special resonance condition called a *zeroth order resonance* is a peculiar phenomenon that can be exploited to maintain the same signal phase throughout the extent of the TL as if it has an *infinite wavelength* [12]. With the assistance of mechanical control, dynamic phase shifting with CRLH TLs has also

been proposed [13]. One of the main applications for which CRLH TLs are considered, however, is as natural leaky wave antennas (LWAs) [5].

A couple of application cases in which CRLH stripline feed networks have the potential to be particularly useful have been identified and are explored here in dedicated chapters. These are: Series feed networks for linear FSAAs, discussed in Chapter 4; feed networks of 2D FSAAs implemented with CRLH stripline and LWAs, which enable an exciting space mapping capability, discussed in Chapter 5; and wideband phase shifters for phase slope manipulation, discussed in Chapter 6. In each of these application Chapters an overview of existing related work in the given application is provided, followed by the contributions that have been validated either by measured performance of fabricated prototypes or solely by accurate electromagnetic simulations.

To build prototypes with the fabrication resources available at Syracuse University, a via-less stripline implementation of a CRLH TL was developed and is presented in Chapter 3, prior to the applications discussions.

Two Chapters are dedicated to provide insight into the process that lead to this dissertation and can be useful for individuals planning to carry out research in related topics or those who wish to fabricate themselves the sort of stripline prototypes presented in this work. An outline of the general methodology adopted is available in Chapter 7 and the main challenges of the fabrication process are discussed in Chapter 8 (Manufacturing Considerations).

A conclusion is provided in Chapter 9 that summarizes the contributions presented throughout the dissertation and proposes ideas for possible future research.

## CHAPTER 2

### FUNDAMENTAL TOPICS

#### 2.1 Metamaterials

The term metamaterial refers to materials that present electromagnetic properties that are not found in nature. In general, when considering the permittivity ( $\epsilon$ ) and permeability ( $\mu$ ), materials can be part of one of the four quadrants of the permittivity versus permeability chart shown in Fig. 2.1. Most common materials that we experience have positive permittivity ( $\epsilon > 0$ ) and permeability ( $\mu > 0$ ). Some materials can naturally present either negative permittivity ( $\epsilon < 0$ ), such as plasmas, or negative permeability ( $\mu < 0$ ), such as gyrotropic materials. Materials that possess both negative permittivity and permeability ( $\epsilon < 0$  and  $\mu < 0$ ), first envisioned by [15], are not encountered in nature but these effects can

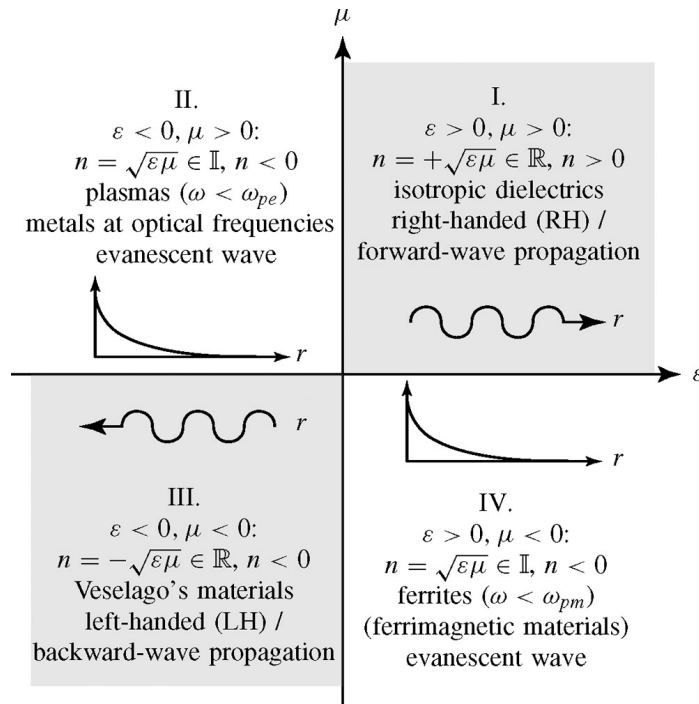


Figure 2.1: Materials characterized by permittivity and permeability. Figure reproduced from [14].

be observed at a macro scale over limited frequency bands through artificial structures. In these cases they are actually *effective* properties ( $\epsilon_{eff}$  and  $\mu_{eff}$ ), although this distinction is implicit throughout this document.

The term *right-handed material* is used to classify materials with positive permittivity and permeability ( $\epsilon > 0$  and  $\mu > 0$ ) due to the relationship between the direction of the electric field ( $\vec{E}$ ), magnetic field ( $\vec{B}$ ), and wave vector ( $\vec{k}$ ). The wave vector direction is opposite for materials with negative permittivity and permeability ( $\epsilon < 0$  and  $\mu < 0$ ), and as such, they can be called *left-handed materials*. Materials that present left-handed properties usually only do so over a specific frequency range, which means depending on the frequency they can behave as one of these cases, having thus a left-handed (LH) and a right-handed (RH) region.

## 2.2 Composite Right/Left-Handed Transmission Lines

Within the past 20 years there has been significant research in how to achieve metamaterial properties in structures that can be more easily fabricated. The published work of [16] laid the foundation for achieving this through what is called composite right/left-handed transmission lines. The name comes from the combined effect of a left-handed and right-handed material that can be achieved at higher frequencies because the features necessary are not much smaller than the wavelength.

The basic transmission line model of the unit cell is presented in Fig. 2.2 and differs from the traditional lossless distributed transmission line model by the addition of a series capacitance ( $C_L$ ) and a shunt inductance ( $L_L$ ). In CRLH TLs the values of these unit cell parameters ( $L_R$ ,  $C_L$ ,  $C_R$ , and  $L_L$ ) are tuned to obtain resonances that relate to the start and stop of the LH and RH bands of operation. These regions are in general separate from each other, but the parameters can be tuned such that the RH region starts where the LH region ends, which yields a smooth transition between LH and RH propagation. When this happens the CRLH TLs is said to be *balanced*.

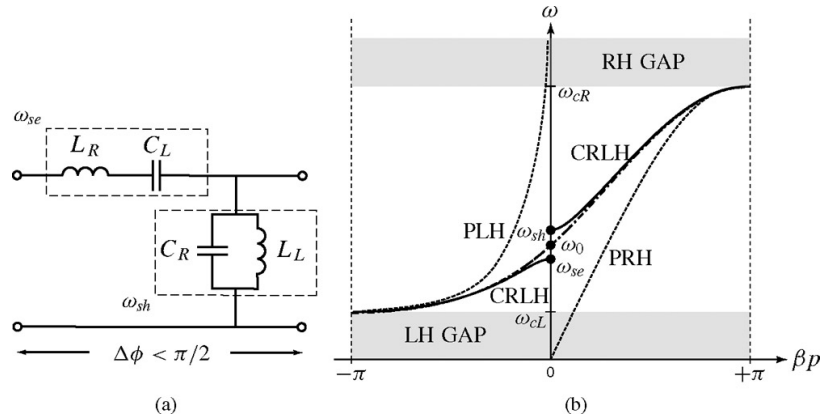


Figure 2.2: a) CRLH unit cell; b) Dispersion diagram. Figure reproduced from [14].

When considering a regular microstrip line, for example, it already presents a distributed series inductance ( $L_R$ ) and shunt capacitance to ground ( $C_R$ ). The typical CRLH unit cell is achieved by adding a series capacitor, such as an interdigital capacitor, and a shunt inductance, through a via to ground. An example is seen in Fig. 2.3.

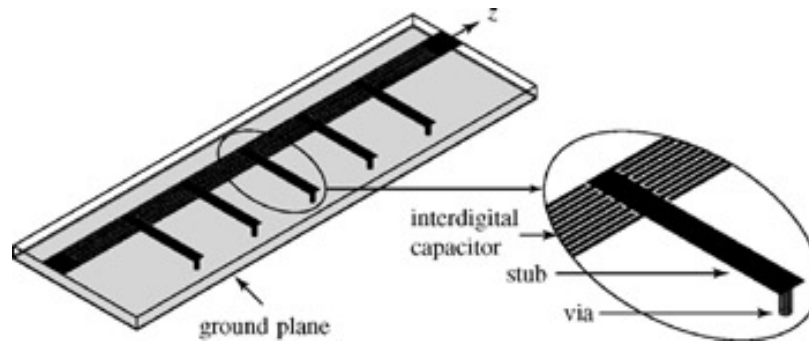


Figure 2.3: Example of microstrip implementation of a CRLH TL including interdigital capacitor and via. Figure reproduced from [14].

### 2.3 Frequency Scanning Antenna Arrays

Frequency scanning antenna arrays are antennas in which the method of steering of the main far field beam is primarily based on the frequency of the signal. This is different than switched beam-forming arrays, such as ones driven by *Butler matrices* or *Rotman lenses*, or phased arrays in which phase is controlled at the antenna elements individually [17].

The illustration in Fig. 2.4 depicts a typical implementation of a FSAA that uses a series

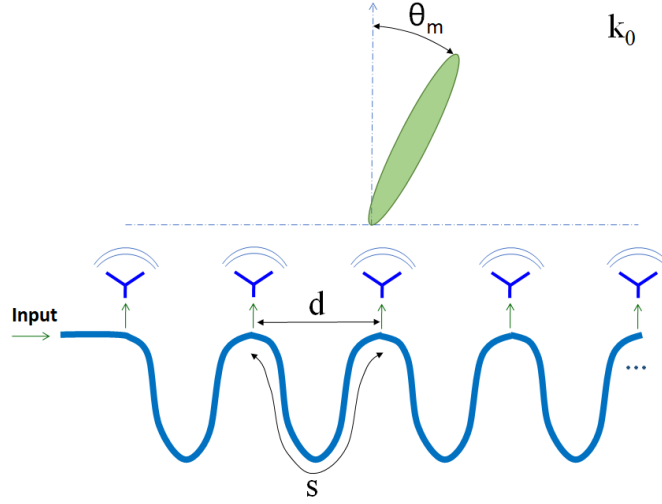


Figure 2.4: Illustration of frequency scanning antenna array with series feed network where  $k_0$  is the wave number in free space,  $d$  is the distance between antennas,  $s$  is the length of transmission line between antennas, and  $\theta_m$  is the direction of far field beam peak off of broadside.

feed network. The transmission line from the feed network naturally provides a phase offset  $\Delta\alpha$  between the antenna elements. As the frequency increases the phase offset increases because the wavelength is decreasing. Taking into account the antenna array theory [18] the in-phase radiation of the antenna elements will constructively add up in the far field culminating into a beam peak. The angular direction  $\theta_m$  of the main beam for the FSAA is given by the following expression:

$$\sin \theta_m = \frac{\Delta\alpha}{k_0 d} \quad (2.1)$$

which means that as the frequency increases, the far field beam peak is steered.

For a feed with transmission line of linear phase dispersion resulting in  $\Delta\alpha$  varying linearly with frequency, the expression can be written in a more common form known as the *frequency-scan equation* [19]:

$$\sin \theta_m = \frac{s\lambda_0}{d} \left( \frac{1}{\lambda_g} - \frac{1}{\lambda_{gm}} \right) \quad (2.2)$$

where  $\lambda_0$  is the wavelength in free space,  $\lambda_g$  is the wavelength in the feed's transmission line, and  $\lambda_{gm}$  is a constant value representing a wavelength of a frequency at which  $s$  is a multiple of  $\lambda_g$ .

The frequency-scan equation is written in a form that emphasizes how the beam steers with frequency relative to the frequency at which the beam is at broadside (the frequency with wavelength  $\lambda_{gm}$ ).

Although the frequency-scan equation above is well known, it is not entirely applicable to the cases explored in this research work because CRLH TLs do not present linear dispersion. For understanding direction of beam peak with CRLH TLs, the expression in Eq.(2.1) is more useful.

The half-power beamwidth of an antenna array is inversely proportional to its antenna aperture, that is, the distance between the antennas at the extremities of the array. The power radiated by each antenna element in an FSAA is typically lower than the previous one because of loss in propagation through the feed line between elements, but also because part of the energy was radiated by the previous element. In order to make better use of the aperture of the antenna and obtain narrower beamwidths, care must be taken at the points where power is coupled to the antennas, such that enough energy can be reached at the elements at the other end of the feed line. Note that the amplitude distribution of an antenna array affects other parameters, such as gain and sidelobe levels, that can be taken into account.

## CHAPTER 3

### THE VIA-LESS COMPOSITE RIGHT/LEFT-HANDED STRIPLINE

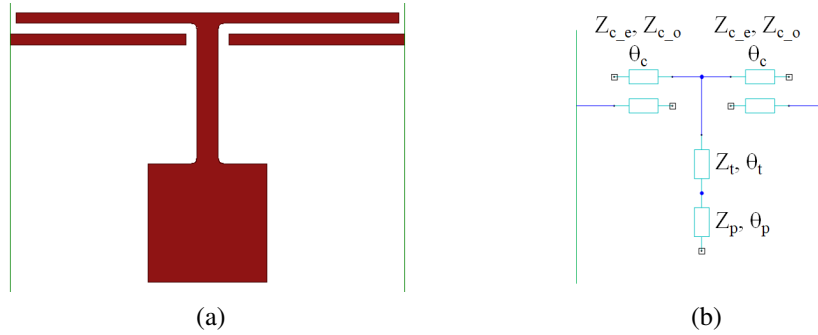


Figure 3.1: Via-less CRLH unit cell. (a) Top view of unit cell in modeler. (b) Schematic of unit cell.

The via-less CRLH unit cell depicted in Fig. 3.1(a), as will be seen, has been used extensively throughout this research in the topic. The traditional CRLH unit cell, as in the one depicted in the CRLH TL in Fig. 2.3, makes use of vias to achieve the shorting of the stub to ground. This is not an issue when implementing a microstrip CRLH because both top and bottom metal layers are easily accessible for soldering. In the case of a stripline fabrication process, the vias are soldered after the substrate and superstrate have been bonded together, at which point the center conductor is not accessible for soldering. It is very difficult to guarantee a good connection of the via to the center conductor without industrial processes and this is likely one of the reasons that stripline technology is not more common in research, even though striplines are quite standard in military applications.

The schematic of the unit cell is presented in Fig. 3.1(b) and, as can be seen, is composed of a pair of coupled transmission lines and an open stub with two-sections. It is interesting to note that without the open stub, the unit cell reduces to that of a half-wavelength parallel (edge) coupled filter [20] which presents right-handed transmission properties. The addition of the stub introduces a left-handed propagation frequency band, as will be seen

in the application Chapters 4 and 5, allowing it to provide phase advancement and delay even though it does not follow the traditional CRLH circuit model in literature constituted of lumped capacitors and inductors ( $L_R$ ,  $C_L$ ,  $C_R$ , and  $L_L$ ) depicted in Fig. 2.2.

### 3.1 Analysis of the Via-Less Composite Right/Left-Handed Transmission Line

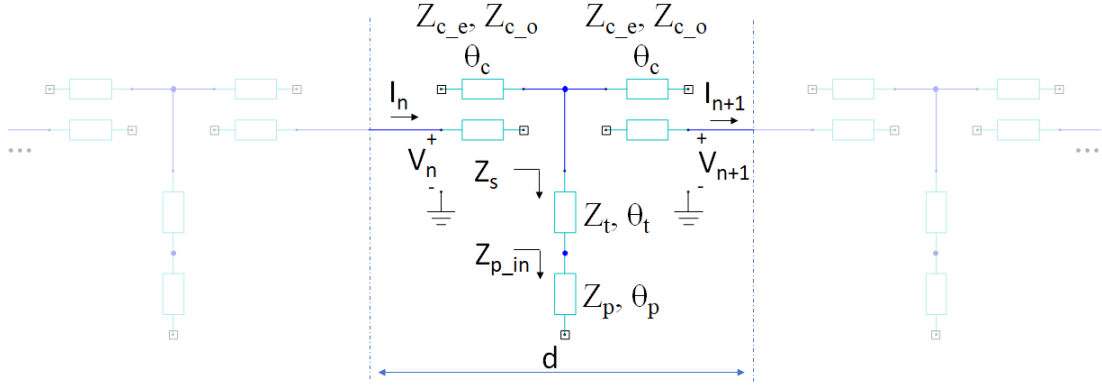


Figure 3.2: Schematic of via-less CRLH unit cell as part of infinitely long periodic transmission line.

An analysis of the base Via-less CRLH stripline cell structure in Fig. 3.1 has been performed in an attempt to better understand its functionality. The analysis method utilized was based on the process outlined in [21] and is not strictly limited to striplines since it is based on general ideal lossless transmission lines.

First the unit cell is assumed to be part of a cascaded infinitely long transmission line, as shown in Fig. 3.2. Due to the periodic nature of the structure, the voltages and currents at the end of the cell is related to the voltages and currents at the beginning of the cell by an attenuation factor  $\alpha$  and a phase offset  $\beta$ . This relation can be exploited as boundary conditions to predict the passbands and bandgaps of the infinitely long transmission line. It is convenient to express the performance of the unit cell circuit in terms of the ABCD network parameters. The reason for this is that this form of network parameters can be easily used to predict performance of cascaded structures by simple matrix multiplications of the matrices that represent the performance of each individual structure [21]. This is

in contrast to Z (impedance), Y (admittance), S (scattering), and T (transmission) network parameters.

The ABCD network parameters for the unit cell are be defined, referring to Fig. 3.2, as:

$$\begin{bmatrix} V_n \\ I_n \end{bmatrix} = [ABCD]_{cell} \begin{bmatrix} V_{n+1} \\ I_{n+1} \end{bmatrix}$$

$$\begin{bmatrix} V_n \\ I_n \end{bmatrix} = \begin{bmatrix} A_{cell} & B_{cell} \\ C_{cell} & D_{cell} \end{bmatrix} \begin{bmatrix} V_{n+1} \\ I_{n+1} \end{bmatrix} \quad (3.1)$$

Defining the wave propagation constant  $\gamma = \alpha + j\beta$ , the infinitely long periodic transmission line will have the previously discussed relation between the voltages at the unit cell extremities:

$$\begin{bmatrix} V_{n+1} \\ I_{n+1} \end{bmatrix} = \begin{bmatrix} e^{-\gamma d} & 0 \\ 0 & e^{-\gamma d} \end{bmatrix} \begin{bmatrix} V_n \\ I_n \end{bmatrix}$$

or

$$\begin{bmatrix} V_n \\ I_n \end{bmatrix} = \begin{bmatrix} e^{\gamma d} & 0 \\ 0 & e^{\gamma d} \end{bmatrix} \begin{bmatrix} V_{n+1} \\ I_{n+1} \end{bmatrix} \quad (3.2)$$

where  $d$  is the physical length of the unit cell.

Subtracting Eq.(3.2) from Eq.(3.1):

$$\begin{bmatrix} A_{cell} & B_{cell} \\ C_{cell} & D_{cell} \end{bmatrix} \begin{bmatrix} V_{n+1} \\ I_{n+1} \end{bmatrix} - \begin{bmatrix} e^{\gamma d} & 0 \\ 0 & e^{\gamma d} \end{bmatrix} \begin{bmatrix} V_{n+1} \\ I_{n+1} \end{bmatrix} = 0$$

$$\begin{bmatrix} A_{cell} - e^{\gamma d} & B_{cell} \\ C_{cell} & D_{cell} - e^{\gamma d} \end{bmatrix} \begin{bmatrix} V_{n+1} \\ I_{n+1} \end{bmatrix} = 0$$

The expression for the determinant of the matrix above must be equal to zero for a *non-trivial solution*, so:

$$A_{cell}D_{cell} + e^{2\gamma d} - (A_{cell} + D_{cell})e^{\gamma d} - B_{cell}C_{cell} = 0$$

Since  $[ABCD]_{cell}$  represents the *reciprocal network* in Fig. 3.2,  $A_{cell}D_{cell} - B_{cell}C_{cell} = 1$ .

This means, from above, that:

$$e^{2\gamma d} - (A_{cell} + D_{cell})e^{\gamma d} + 1 = 0$$

which can be manipulated to

$$e^{-\gamma d} + e^{\gamma d} = A_{cell} + D_{cell}$$

and eventually

$$\cosh \gamma d = \frac{A_{cell} + D_{cell}}{2} \quad (3.3)$$

and will be used to determine the propagation characteristics from the ABCD network parameters of the unit cell.

These network parameters, as mentioned before, can be obtained by cascading the parameters of the individual sections of the unit cell, as in:

$$[ABCD]_{cell} = [ABCD]_c [ABCD]_s [ABCD]_c \quad (3.4)$$

where  $[ABCD]_c$  are the parameters of the coupled transmission lines sections and  $[ABCD]_s$  are the parameters of the shunt two-section open stub.

The ABCD network parameters of the coupled transmission lines can be obtained through conversion from its impedance network parameters, as discussed in [21] and summarized in its Table 4.2. So we have:

$$[ABCD]_c = \begin{bmatrix} \frac{Z_{11c}}{Z_{21c}} & \frac{|Z_c|}{Z_{21c}} \\ \frac{1}{Z_{21c}} & \frac{Z_{22c}}{Z_{21c}} \end{bmatrix}$$

or

$$\begin{aligned} A_c &= \frac{Z_{11c}}{Z_{21c}} \\ B_c &= \frac{|Z_c|}{Z_{21c}} \\ C_c &= \frac{1}{Z_{21c}} \\ D_c &= \frac{Z_{22c}}{Z_{21c}} \end{aligned} \quad (3.5)$$

where

$$|Z_c| = Z_{11c}Z_{22c} - Z_{12c}Z_{21c} \quad (3.6)$$

The impedance network parameters of the coupled transmission lines from Fig. 3.2 are (from Eq.(8.99) in [21]):

$$[Z]_c = \begin{bmatrix} -\frac{j}{2}(Z_{c.e} + Z_{c.o}) \cot \theta_c & -\frac{j}{2}(Z_{c.e} - Z_{c.o}) \csc \theta_c \\ -\frac{j}{2}(Z_{c.e} - Z_{c.o}) \csc \theta_c & -\frac{j}{2}(Z_{c.e} + Z_{c.o}) \cot \theta_c \end{bmatrix}$$

or

$$\begin{aligned} Z_{11c} &= -\frac{j}{2}(Z_{c.e} + Z_{c.o}) \cot \theta_c \\ Z_{21c} &= -\frac{j}{2}(Z_{c.e} - Z_{c.o}) \csc \theta_c \\ Z_{12c} &= -\frac{j}{2}(Z_{c.e} - Z_{c.o}) \csc \theta_c = Z_{21c} \\ Z_{22c} &= -\frac{j}{2}(Z_{c.e} + Z_{c.o}) \cot \theta_c = Z_{11c} \end{aligned} \quad (3.7)$$

where  $Z_{c.e}$  and  $Z_{c.o}$  are the even and odd mode impedances of the coupled transmission lines, respectively, and  $\theta_c$  is the coupled electrical length. It is seen that the symmetry of the coupled lines section leads to simplified parameters. This simplification also applies to

$[ABCD]_c$  and, after taking into account the equality of parameters in Eq.(3.7), can be seen to be:

$$D_c = A_c \quad (3.8)$$

and the  $|Z_c|$  quantity of  $B_c$ :

$$|Z_c| = Z_{11c}^2 - Z_{21c}^2 \quad (3.9)$$

The ABCD network parameters of the center portion of the cell, which is constituted of a shunt two-section open stub, can be obtained through the ABCD network parameters of the two-port circuit with shunt admittance given in Table 4.1 of [21] to be:

$$[ABCD]_s = \begin{bmatrix} 1 & 0 \\ Y_s & 1 \end{bmatrix}$$

or

$$\begin{aligned} A_s &= 1 \\ B_s &= 0 \\ C_s &= Y_s \\ D_s &= 1 \end{aligned} \quad (3.10)$$

where  $Y_s$  is the input admittance of the stub.

The input admittance of the two-section open stub is the inverse of its input impedance. As seen in Fig. 3.2, the input impedance of the open stub is given by the *transmission line impedance equation* when considering the load to be an open circuit. This would be (based on Eq.(2.46c) of [21]):

$$Z_{pin} = -jZ_p \cot \theta_p \quad (3.11)$$

where  $Z_p$  and  $\theta_p$  are the characteristic impedance and electrical length of that open stub. The subscript  $p$  is used because this open stub is usually wide and its aspect ratio makes

it resemble a pad. The input impedance  $Z_s$  of the whole two-section stub is then obtained through the transmission line impedance with  $Z_{pin}$  as the load:

$$Z_s = Z_t \frac{Z_{pin} + jZ_t \tan \theta_t}{Z_t + jZ_{pin} \tan \theta_t} \quad (3.12)$$

where  $Z_t$  and  $\theta_t$  are the characteristic impedance and electrical length of the section prior to the open stub, which effectively transforms its impedance.

Inverting, to arrive at the admittance, and substituting  $Z_{pin}$  from Eq.(3.11):

$$Y_s = \frac{1}{Z_s} = \frac{1}{Z_t} \frac{Z_t + jZ_{pin} \tan \theta_t}{Z_{pin} + jZ_t \tan \theta_t}$$

$$Y_s = \frac{j Z_t + Z_p \cot \theta_p \tan \theta_t}{Z_t Z_p \cot \theta_p + Z_t \tan \theta_t} \quad (3.13)$$

With the expressions for the ABCD network parameters of the sections that constitute the unit cell, the cascaded ABCD network parameters can be determined by carrying out the matrix multiplications in Eq.(3.4):

$$\begin{bmatrix} A_{cell} & B_{cell} \\ C_{cell} & D_{cell} \end{bmatrix} = \begin{bmatrix} A_c & B_c \\ C_c & D_c \end{bmatrix} \begin{bmatrix} A_s & B_s \\ C_s & D_s \end{bmatrix} \begin{bmatrix} A_c & B_c \\ C_c & D_c \end{bmatrix} \quad (3.14)$$

Substituting the values from Eq.(3.10) in order to simplify the multiplication:

$$\begin{bmatrix} A_{cell} & B_{cell} \\ C_{cell} & D_{cell} \end{bmatrix} = \begin{bmatrix} A_c & B_c \\ C_c & D_c \end{bmatrix} \begin{bmatrix} 1 & 0 \\ Y_s & 1 \end{bmatrix} \begin{bmatrix} A_c & B_c \\ C_c & D_c \end{bmatrix}$$

$$= \begin{bmatrix} A_c + B_c Y_s & B_c \\ C_c + D_c Y_s & D_c \end{bmatrix} \begin{bmatrix} A_c & B_c \\ C_c & D_c \end{bmatrix}$$

$$\begin{bmatrix} A_{cell} & B_{cell} \\ C_{cell} & D_{cell} \end{bmatrix} = \begin{bmatrix} A_c^2 + A_c B_c Y_s + B_c C_c & A_c B_c + B_c^2 Y_s + B_c D_c \\ A_c C_c + A_c D_c Y_s + C_c D_c & B_c C_c + B_c D_c Y_s + D_c^2 \end{bmatrix}$$

or

$$\begin{aligned} A_{cell} &= A_c^2 + A_c B_c Y_s + B_c C_c \\ B_{cell} &= A_c B_c + B_c^2 Y_s + B_c D_c \\ C_{cell} &= A_c C_c + A_c D_c Y_s + C_c D_c \\ D_{cell} &= B_c C_c + B_c D_c Y_s + D_c^2 \end{aligned} \tag{3.15}$$

where, considering Eq.(3.8), the following additional simplification can be made:

$$D_{cell} = A_{cell} \tag{3.16}$$

Substituting the network parameters from Eq.(3.5) and Eq.(3.10) into the  $A_{cell}$  expression in Eq.(3.15):

$$\begin{aligned} A_{cell} &= \left( \frac{Z_{11c}}{Z_{21c}} \right)^2 + \frac{Z_{11c}}{Z_{21c}} \frac{|Z_c|}{Z_{21c}} Y_s + \frac{|Z_c|}{Z_{21c}} \frac{1}{Z_{21c}} \\ &= \frac{Z_{11c}^2 + Z_{11c} |Z_c| Y_s + |Z_c|}{Z_{21c}^2} \\ &= \frac{Z_{11c}^2 + Z_{11c} (Z_{11c}^2 - Z_{21c}^2) Y_s + Z_{11c}^2 - Z_{21c}^2}{Z_{21c}^2} \\ &= \frac{2Z_{11c}^2 + Z_{11c}^3 Y_s - Z_{11c} Z_{21c}^2 Y_s - Z_{21c}^2}{Z_{21c}^2} \\ &= 2 \frac{Z_{11c}^2}{Z_{21c}^2} - 1 + Z_{11c} \frac{Z_{11c}^2 - Z_{21c}^2}{Z_{21c}^2} Y_s \end{aligned}$$

$$A_{cell} = 2 \frac{Z_{11c}^2}{Z_{21c}^2} - 1 + Z_{11c} Y_s \left( \frac{Z_{11c}^2}{Z_{21c}^2} - 1 \right) \quad (3.17)$$

Substituting the impedance network parameters from the couplers (Eq.(3.7)), the expression becomes

$$A_{cell} = 2 \left( \frac{Z_{c.e} + Z_{c.o}}{Z_{c.e} - Z_{c.o}} \right)^2 \cos^2 \theta_c - 1 + \frac{(Z_{c.e} + Z_{c.o}) (Z_t + Z_p \cot \theta_p \tan \theta_t)}{2Z_t \frac{Z_p \cot \theta_p - Z_t \tan \theta_t}{Z_p \cot \theta_p - Z_t \tan \theta_t}} \cot \theta_c \left[ \left( \frac{Z_{c.e} + Z_{c.o}}{Z_{c.e} - Z_{c.o}} \right)^2 \cos^2 \theta_c - 1 \right] \quad (3.18)$$

The expression Eq.(3.3) can then finally be used to determine the passband and bandgaps of this infinitely long cascaded transmission line. For this, the left hand side of Eq.(3.3) can be expanded, as in

$$\cosh \gamma d = \cosh (\alpha + j\beta) d = \cosh \alpha d \cos \beta d + j \sinh \alpha d \sin \beta d \quad (3.19)$$

Using Eq.(3.16) for substitution into the right-hand side of Eq.(3.3):

$$\cosh \alpha d \cos \beta d + j \sinh \alpha d \sin \beta d = \frac{2A_{cell}}{2} = A_{cell} \quad (3.20)$$

Since  $A_{cell}$  in Eq.(3.18) has no imaginary component, the following requirement must be met according to the expression above:

$$\sinh \alpha d \sin \beta d = 0 \quad (3.21)$$

This requirement can be met for  $\beta = \pm \frac{m\pi}{d}$ ,  $m = 0, 1, 2, \dots$ ,  $\alpha \neq 0$  in which case the wave is attenuated and, due to the infinitely long nature of the analysis, defines the bandgap of the transmission line. When  $\alpha = 0, \beta \neq 0$ , the wave is not attenuated and propagation

occurs if

$$\cos \beta d = A_{cell} \quad (3.22)$$

is valid, which occurs when

$$|A_{cell}| \leq 1 \quad (3.23)$$

For infinitely long periodic structures the concept of Bloch impedance is used to represent the effective relationship between voltage and currents taking into account all the reflections within the cell. This impedance can be determined from the ABCD network parameters of the unit cell and is given by [21]:

$$Z_{B_{cell}} = \frac{B_{cell}}{\sqrt{A_{cell}^2 - 1}} \quad (3.24)$$

### 3.2 Passbands Determination

From the analysis in the previous section, it is determined that the unit cell is capable of propagating a wave for frequencies that meet the following criteria:

$$\left| 2 \left( \frac{Z_{c,e} + Z_{c,o}}{Z_{c,e} - Z_{c,o}} \right)^2 \cos^2 \theta_c - 1 + \frac{(Z_{c,e} + Z_{c,o})(Z_t + Z_p \cot \theta_p \tan \theta_t)}{2Z_t} \cot \theta_c \left[ \left( \frac{Z_{c,e} + Z_{c,o}}{Z_{c,e} - Z_{c,o}} \right)^2 \cos^2 \theta_c - 1 \right] \right| \leq 1 \quad (3.25)$$

This passband conditional testing above for this via-less CRLH TL has been implemented in a Matlab computer code that takes the various characteristic impedances and electrical lengths of the unit cell in Fig. 3.2 and displays the passbands up to 20 GHz. The computer code is available in the Appendix A.

The code's results have been compared with that of circuit simulator models to validate its functionality. As expected, as the number of unit cells included in the circuit simulator

model increases, the closer its passband response matches that of the code. The reason for this is that by increasing the number of cells, the closer those simulation models get to the infinite cascaded unit cell case considered for the analysis in Section 3.1.

Although the passband of the unit cell can be determined by the expression in Eq.(3.25), the relationship between the parameter quantities and the passband properties are not obvious. Additionally, there are other aspects encountered in the actual implementation environment that affect these passbands. First, there is the finite nature of an actual implementation. Circuit simulators can be used to better predict the passband performance based on such finite cascaded unit cells transmission lines. Second, the parasitic effects in the various transitions (impedance step as well as T junction) and open stubs (including those of the couplers) significantly shift the passbands in practice. The use of a 3D electromagnetic full wave solvers is a good solution for these. Furthermore, in some cases the materials used in fabrication are not electrically isotropic, as will be seen to be the case of the materials used in this research. 3D electromagnetic solvers are better suited than current circuit simulators to predict the effective electrical properties due to these anisotropic materials.

### 3.3 Design Procedure

The recommended method to design a CRLH transmission line based on this unit cell is to first create a 3D EM model of a single unit cell and use the *eigenmode solver* from the 3D EM tool to determine its dispersion characteristics. Eigenmode solvers are able to determine the resonant modes of a structure under specified boundary conditions. To determine the dispersion characteristics this way, the unit cell model should be enclosed between two boundaries (one at the beginning of the unit cell and one at its end) that maintain a master/slave [22] relation, that is, the solver will enforce the same field distribution at the two boundaries, with the exception of a phase offset  $\theta_{offset}$  between them that can be specified. These types of boundaries are sometimes referred to as periodic boundaries [23], and can be expressed as:

$$\bar{E}_{slave} = \bar{E}_{master} e^{j\theta_{offset}}$$

The eigenmode analysis yields the frequencies and fields that can exist under these boundary conditions. By solving the model for various phase offsets ( $0^\circ \leq \theta_{offset} \leq 180^\circ$ ) and plotting the frequencies of the proper propagating modes found, the dispersion of the infinite cascaded unit cell case can be accurately determined [24]. Tuning the parameters of the unit cells will allow, to an extent, arbitrary manipulation of the left-handed and right-handed passbands. Once a satisfied dispersion characteristic is attained, the unit cell can then be included into a model of where it will be used and be driven by excitations. The characteristic impedance can be matched through the use of a quarter-wave impedance transformer which will add little to a CRLH TL of significant length. If the characteristic impedance of the CRLH TL needs to be changed, it is likely that a material with different properties, as in permittivity and thicknesses, will be needed. A slight adjustment may be needed to the unit cell at this point due to the finite nature of the application.

## CHAPTER 4

### FEED NETWORKS FOR LINEAR FREQUENCY SCANNING ANTENNA ARRAYS

Traditional series feed networks are used to provide beam steering capability to antenna arrays based on the transmission frequency. Their steering capability only scans naturally from near broadside to end-fire due to the right-handed-only properties of regular transmission lines but they usually take advantage of phase wrapping of longer lines to provide back-fire to end-fire steering capability. In these cases the transmission lines often require meandering (serpentine lines) due to size [25].

Several types of CRLH TLs have been proposed for use in frequency scanning antenna array applications (with one group's summary outlined in [5]). CRLH TLs, with their dual phase velocity behavior [11], can be used as leaky-wave antennas (with radiation mechanism discussed nicely by [26]) for frequency beam steering from back-fire to end-fire [27]. They can be made quite compact assuming the necessary reactances are achievable by the manufacturing process [11]. Solutions based on substrate integrated waveguides (SIWs) have also been presented [8]. One limitation, however, is that they are limited to the antenna radiation characteristics of the unit cell.

A lumped element CRLH feed network presented in [4] addresses most of the limitations mentioned. Its lumped element nature, however, prevents its operation above around 5 GHz due to the increasing reactances of the package parasitics as the frequency increases. Additionally, its corporate topology is not very compact.

The concept of a series feed network is discussed next in which the phase progression is achieved by a distributed CRLH TL stripline and has been presented in [28]. The radiative nature of a CRLH TL (which is why they are used as leak- wave antennas) is avoided since stripline technology is used.

## 4.1 Feed Network Using Via-Less CRLH Stripline Unit Cell

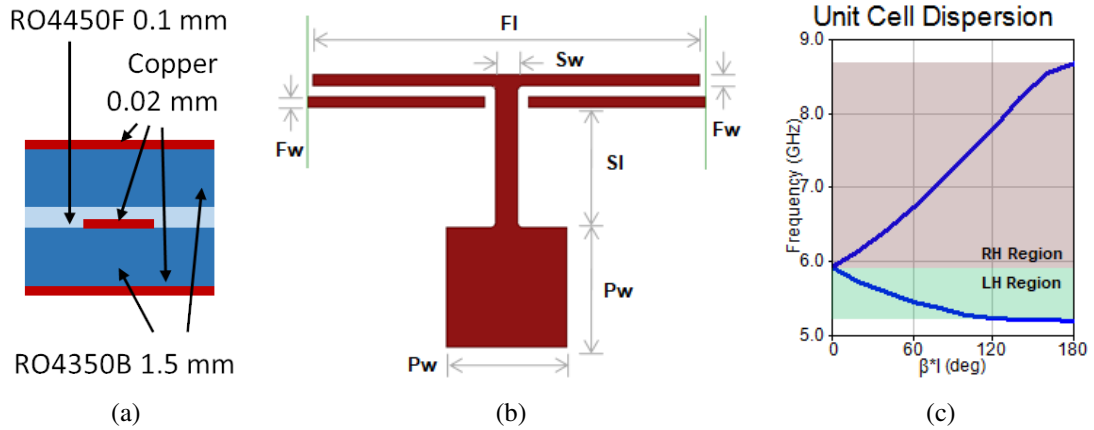


Figure 4.1: Stripline CRLH unit cell with stub to open patch. (a) Stripline stackup. (b)  $Fl = 355$  mils,  $Fw = 10$  mils,  $Sw = 20$  mils,  $Sl = 110$  mils,  $Pw = 110$  mils and all gaps = 10 mils. (c) 3D EM simulated dispersion curve.

### 4.1.1 Unit Cell

The design of the feed network begins with the CRLH unit cell. The desire for a continuous scanning frequency range leads us to a balanced CRLH unit cell requirement. This means that the  $\beta = 0$  frequency of both the LH and RH region must be tuned to the same frequency [11], preventing a bandgap between them. The tuning of the unit cell presented here was done solely based on 3D EM simulation and sensitivity analysis to its parameters. The unit cell utilized is of the type discussed in Chapter 3 and can be seen in Fig. 4.1(b). A similar unit cell has been presented [29] and is useful here since there is no added sensitivity to via positioning. The via connection reliability uncertainty of our current manufacturing capabilities also led us to this vialess cell.

It is important to note that the substrate chosen for this stackup is composed of fiber glass weaves. These glass weaves improve the sturdiness of the board which is a benefit for this application but it presents a drawback in that it introduces anisotropic effective permittivity. This is due to the fact that fiber glass cloth is weaved along the plane of the

substrate sheet. Electric field components aligned to this plane are greatly influenced by the permittivity of the fiber glass, whereas the electric fields perpendicular to it are primarily influenced by the permittivity of the resin of the substrate. Since the permittivity of the fiber glass is different than that of the resin that composes the remainder of the substrate, the effective permittivity in the two Cartesian axii in the plane of the sheet is lower than the one in the axis perpendicular to it, making this substrate a *positive uniaxial* medium [30]. A generic analysis method of the effects of woven glass is available [31], but the values used for simulation throughout this work were obtained from [32] that specifically measured the permittivity anisotropy of RO4350B through an iterative method that compares resonances obtained in simulation of edge coupled lines in an uniaxial medium with those measured from a test unit. Using the *permittivity tensor* notation from [30], the relationship between the electric field  $\bar{E}$  and the electric displacement  $\bar{D}$  used for RO4350B throughout this work is:

$$\bar{D} = \bar{\epsilon} \cdot \bar{E} \quad (4.1)$$

where

$$\bar{\epsilon} = \begin{bmatrix} \epsilon_{plane} & 0 & 0 \\ 0 & \epsilon_{plane} & 0 \\ 0 & 0 & \epsilon_{perpendicular} \end{bmatrix} = \begin{bmatrix} 3.3 & 0 & 0 \\ 0 & 3.3 & 0 \\ 0 & 0 & 3.64 \end{bmatrix} \quad (4.2)$$

The dispersion characteristics of the cell in Fig. 4.1(b) in an infinitely long transmission line can be seen in Fig. 4.1(c). The left-hand region is between 5.2 - 5.9 GHz and the right-hand region is between 5.9 - 8.7 GHz. It is desired that the left-hand region spans a significant frequency range to reduce the frequency sensitivity when exciting an array in this range. When used in a finite transmission line or other structures, the added disconti-

nities present parasitic effects that may slightly put off the balanced response and present a small bandgap. Slight tweaks are then needed to return to a balanced response.

#### 4.1.2 Series Feed

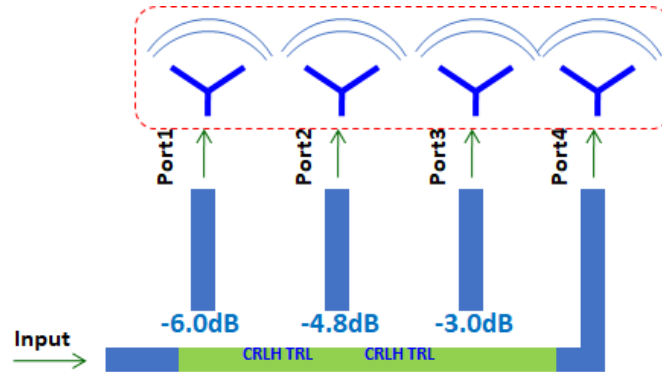


Figure 4.2: Linear FSA general schematic for equal power excitation at 4 ports.

For a series feed the goal was to implement a network as shown in the general schematic shown in Fig. 4.2. The CRLH TL sections, composed of cascaded unit cells, provides the necessary phase offset at specific distance intervals. Power dividing/coupling structures are needed at these locations to tap into the power of the feed. A suitable option for the CRLH TL is the directional coupler proposed in [33]. These behave similarly to a regular edge coupled directional couplers but are able to achieve higher coupling values for similar gaps without the need to resort to broadside coupling. Coupling values of up to 0 dB are possible [33]. A single coupled cell was chosen for minimal size. This leaves the gap between the coupled cells available for coupling tuning. A 4-element series feed requires 3 of such couplers. For an equal amplitude power distribution, the ideal coupling values for each coupler is -6.0 dB, -4.8 dB, and -3.0 dB, in order, as seen in Fig. 4.2. The couplers were tuned individually via simulation to achieve the desired coupling values around the balanced frequency. Good values of directivity were observed during initial simulation of the directional couplers, as seen in the performance of Fig. 4.3(b) for the model in Fig. 4.3(a). Based on these directivity results, the directional couplers were simulated

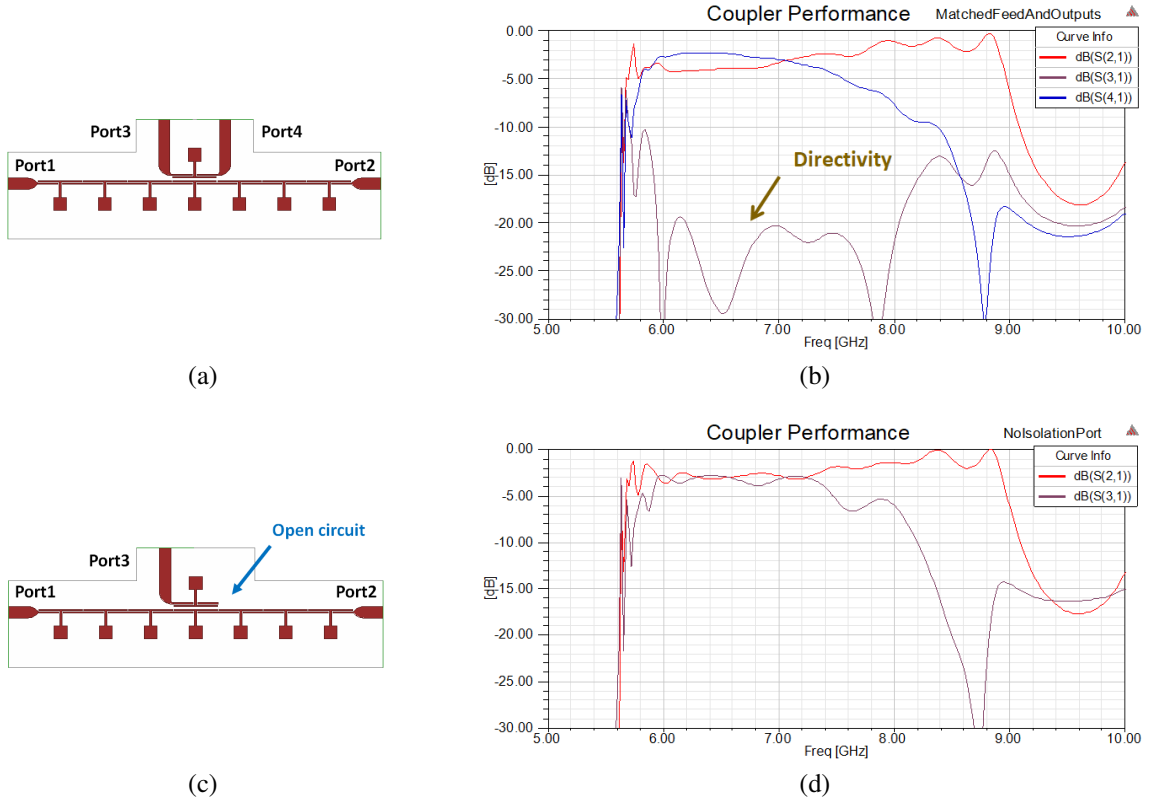


Figure 4.3: Models of preliminary CRLH TL directional couplers. (a) Traditional model with 4-ports. (b) Performance of 4-port model with low directivity. (c) Model with 3-ports in which the directivity port is left as an open circuit. (d) Performance of the 3-port model indicates that the open circuit does not significantly affect the parameters of interest.

with 3-ports, that is, with the directivity port left as open circuit as in Fig. 4.3(c). The performance parameters of interest of the 3-ports model, as exemplified in Fig. 4.3(d) were not significantly affected. The 3-port version provides a much simpler fabrication approach since terminating loads are not needed in the design. These 3-port models were therefore selected.

Attention must be given to the phase dispersion of the final port, which comes out straight from the CRLH TL with no coupling as in Fig. 4.4(a). The signal to this port does not receive the wideband  $+90^\circ$  phase offset provided by the directional couplers on the other ports. Phase match could be achieved at the balanced frequency with a regular transmission line but it does not provide the wideband dispersion desired for that final port, as seen in Fig. 4.4(b). Instead, if an additional CRLH cell is used as in the network in

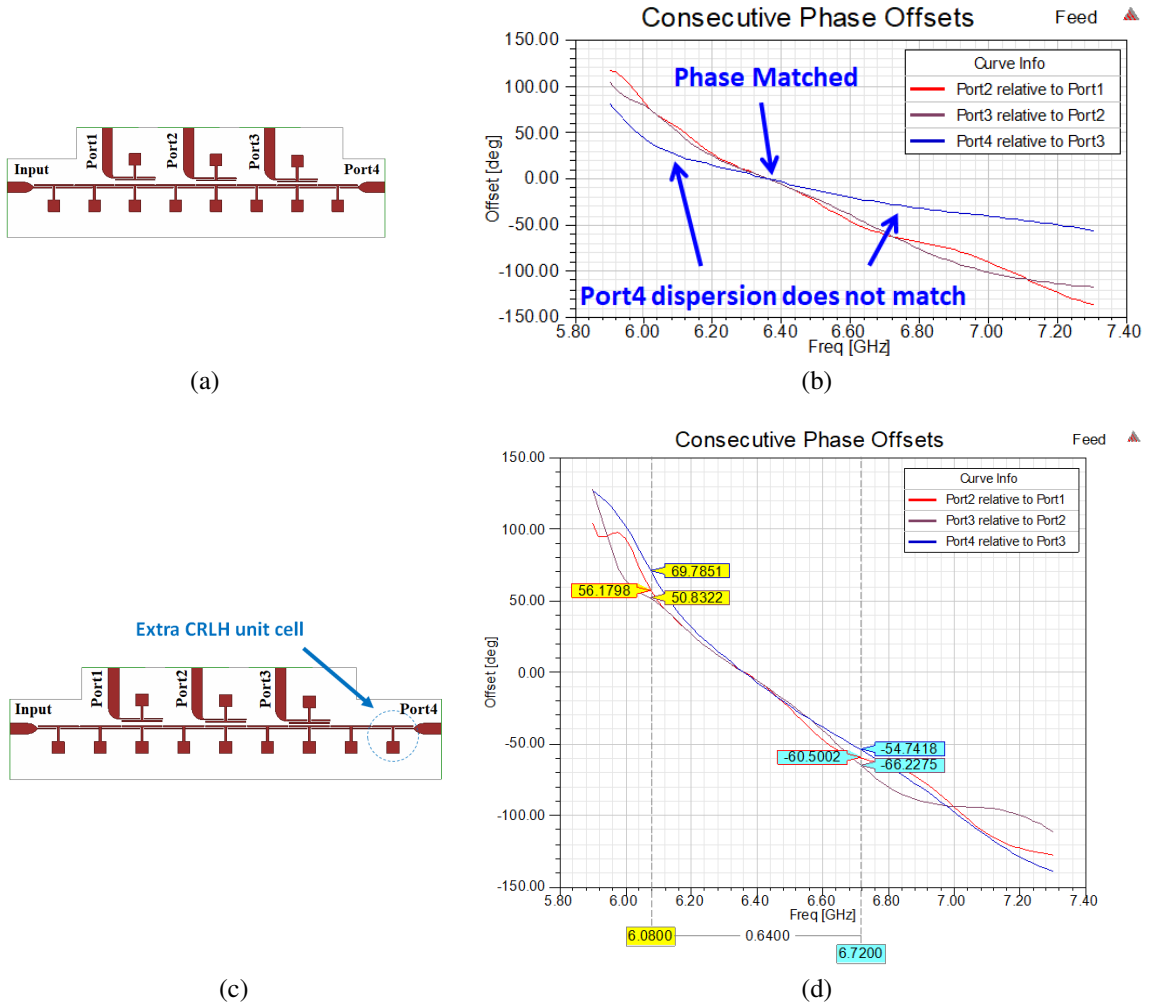


Figure 4.4: Models of preliminary CRLH stripline feed networks with different paths for last port. (a) Model with Port4 immediately after last directional coupler. (b) Phase progression of model in (a). (c) Model with extra CRLH unit cell on Port4 path. (d) Phase progression of model in (c).

Fig. 4.4(c), a better match in the dispersion is achievable for the phase matched case (see Fig. 4.4(d)). The final feed network model is presented in Fig. 4.5. The simulated input return loss, output power through ports, and progressive output ports phase offsets can be seen in Fig. 4.6(a), Fig. 4.6(b), and Fig. 4.6(c), respectively.

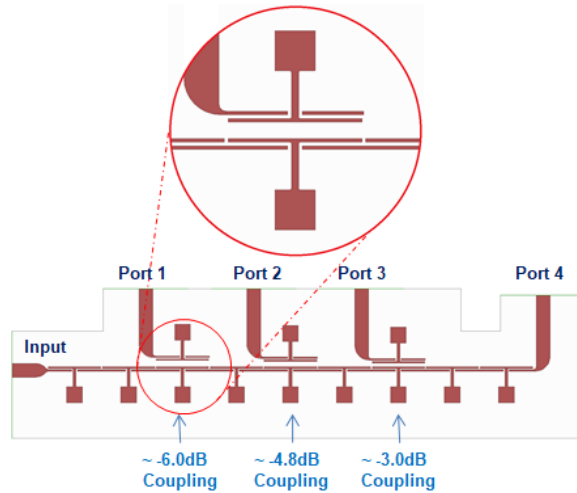


Figure 4.5: Stripline CRLH feed network model.

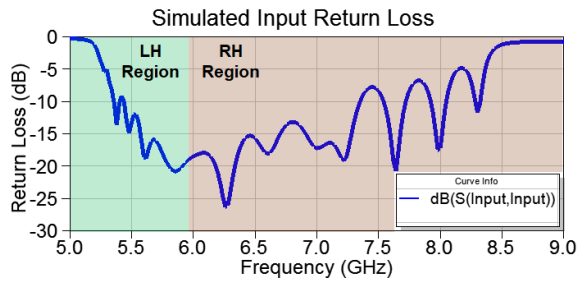
## 4.2 Prototype

### 4.2.1 Design

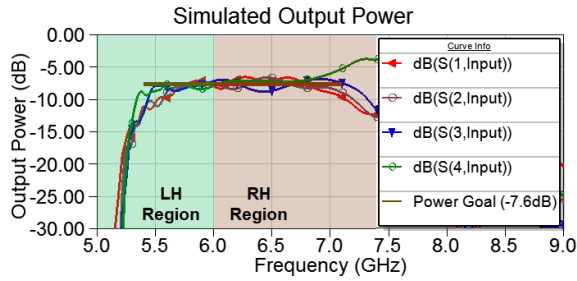
A prototype of the 4-element feed network was built in our lab (Fig. 4.7(a) and Fig. 4.7(b)). The board measures 4.6''x2.5''x0.122'' (without the connectors) and includes  $\lambda/4$  impedance transformers at all ports, as well as phase matching lines to the outputs. The transformers are needed to match the system characteristic impedance of  $50\Omega$  for excitation and measurements. In an integrated scenario, antenna elements would be designed to match the network, levying the need of transformation at the outputs. The phase matching lines are necessary primarily due to the position of the reference plane of the last port relative to the coupled ports. This prototype has the element spacing rounded to 0.75'' which is slightly under the feed network output spacing of 0.754''.

### 4.2.2 Measurements Results

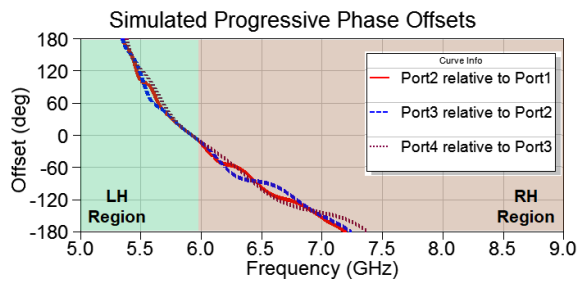
The prototypes input return loss and output powers can be seen in Fig. 4.8(a) and Fig. 4.8(b), respectively. From Fig. 4.8(a) it is seen that it presents a worse return loss than predicted in simulation. The through powers in Fig. 4.8(b) also vary from prediction. The overall



(a)

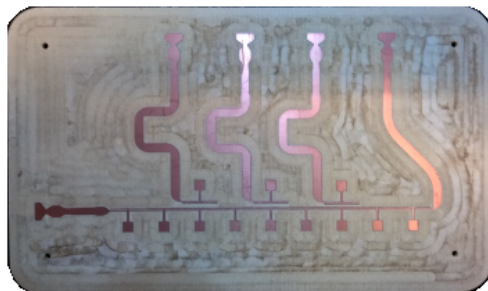


(b)



(c)

Figure 4.6: Simulation results of model in Fig. 4.5. (a) Input return loss. (b) Output power. (c) Progressive phase offset of output ports - Port  $x$  relative to port  $y$  defined as  $\angle(S(x,Input)/S(y,Input))$ .

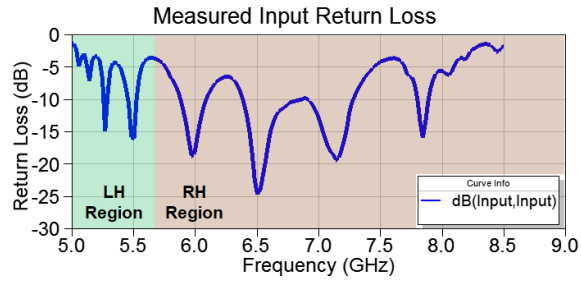


(a)

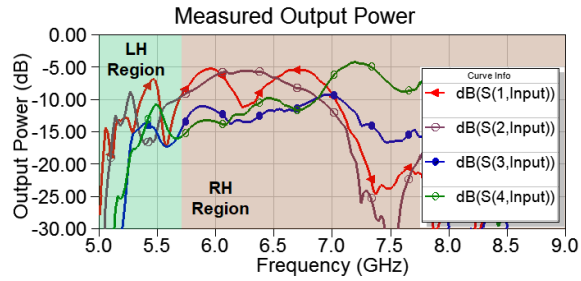


(b)

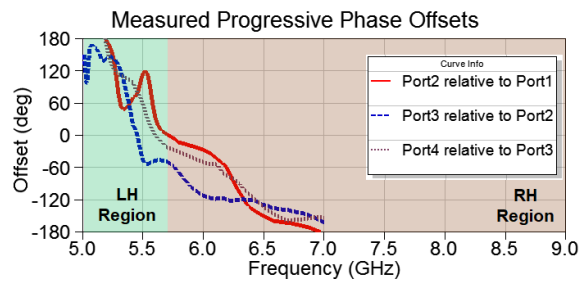
Figure 4.7: Stripline prototype. (a) Bottom substrate prior to lamination. (b) Feeding antenna array in measurement setup.



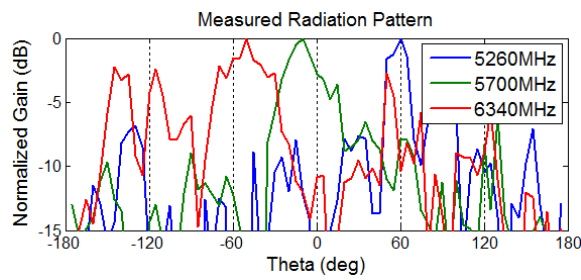
(a)



(b)



(c)



(d)

Figure 4.8: Measured results from prototype in Fig. 4.7. (a) Input return loss. (b) Output power. (c) Progressive phase offset of output ports. (d) Radiation pattern of select frequencies (s at  $\theta = 0^\circ$ ).

bandwidth and power division of the feed network, however, can be clearly confirmed. The progressive phase offsets of the output ports were calculated from the data and are presented in Fig. 4.8(c). A big variation can be seen over some frequency ranges and a left-hand re-

gion is observed, albeit shifted to lower in the spectrum. The main sources of discrepancies between simulation and measurements are primarily manufacturing-related since this was the first laminated stripline made by our research group in-house. Quasi-Yagi-like antennas were fabricated for measurement of the radiation pattern of the prototype. The assembled array can be seen in Fig. 4.7(b). Fig. 4.8(d) presents the pattern measured in the plane of the prototype. Beam steering capability can be identified to both sides of the broadside angle. These results may be further improved by minimizing fabrication errors and misalignment of the antenna elements.

### **4.3 Summary**

The concept of a series feed network that uses distributed CRLH TL and couplers has been presented and demonstrated by the measurements of a built prototype. The radiated beam, when exciting an antenna array, is steerable from back-fire to end-fire, which is not possible with a traditional series feed network. To cover the same beam angles, a traditional network would need special routing, be longer relative to this CRLH version, and possibly need various coupling mechanisms to achieve the range of output coupling required, thus complicating the design. The stripline design prevents undesired radiation inherent to distributed CRLH TLs, and being a feed network allows flexibility in the choice of the antenna to whichever best meets the given array application requirements.

## CHAPTER 5

### FEED NETWORKS FOR 2D FREQUENCY SCANNING ANTENNA ARRAYS

Modern antenna array systems with beam steering capability have, in many cases, moved from mechanical to electrical beam steering. The steering is often accomplished by dynamically controlling the excitation of the antenna elements by means of tunable phase shifters and attenuators. The cost, size and processing power required to implement these sort of control mechanisms can be significant and the industry and research community continue to search for compact and affordable solutions, particularly for potentially high volume consumer applications.

The rise of metamaterials and CRLH TLs [14] has contributed to significant advancements in this area. Various companies in industry started developing, and even commercializing, products that control material properties for beamforming, for example, in satellite communication, and radars for unmanned aerial vehicles and automotives [34]. These technologies, however, still require a significant amount of beam control mechanisms.

The concept explored here is the use of CRLH TLs for miniaturization of frequency scanning antenna arrays. Traditional FSAs rely on a straightforward principle to steer beams. They are not ideal for communication applications due to limited signal bandwidth in a given direction, but can be extended to be good options for low cost imaging [35, 36] and radar applications [37–39]. Typically, separate FSAs are used for azimuth and elevation [35, 36]. Some methods of using CRLH TLs as leaky wave antennas (LWAs) for space mapping have been proposed, as in [40] which requires additional phase control mechanism, and in [41] which must process signals from many separate LWAs.

Our approach, originally outlined in [42] and depicted by the diagram in Fig. 5.1, is aligned with the spectral decomposition concept by CRLH TLs introduced in [43]. By interconnecting linear FSAs with a progressive phase feed network, an array system can

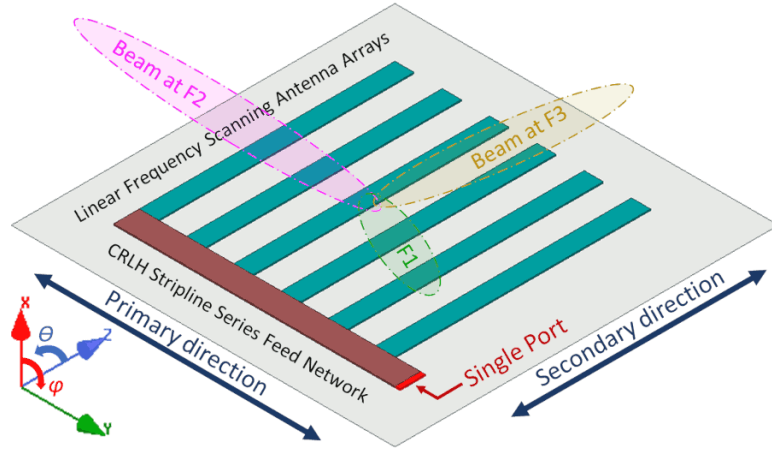


Figure 5.1: Diagram of the proposed 2D Frequency Scanning Array.

map frequencies at its single port to angular coordinates (or spatial angles) in the radiating hemisphere. The whole visible space can then be mapped in real-time. By using a series feed network topology and implementing the phase progression through a CRLH stripline, a significant reduction in size can be achieved compared to a corporate feed with phasers [43] or even CRLH microstrip lines [44], and especially compared to the use of traditional TLs. An integrated solution is introduced with a reduced footprint CRLH stripline feed network that does not affect radiation performance [45]. The design process is detailed to provide better understanding of the considerations needed in the design of such system.

## 5.1 Design

The general concept in this design relies on a progressive phase series feed in the primary direction, connected to several linear FSAs in the secondary direction, as proposed in [42]. One of the directions is selected to have a high phase progression and it is convenient for the primary direction be selected for this (for several reasons discussed in the next section). An example of the desired phase progression relationship between the feed network and linear arrays can be seen in Fig. 5.2. As for the beam steering, the linear arrays allow a single scanning sweep in the secondary direction, and the high progressive phase network ensures multiple scanning sweeps in the primary direction. The combined scan-

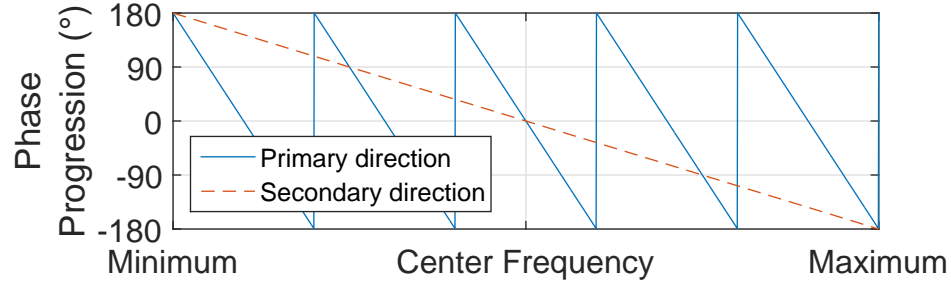


Figure 5.2: Phase progression relationship between directions. The feed network is in the primary direction and the linear arrays are in the secondary direction.

ning effect is that of a raster scan of space, in which the number of passes is determined by the amount of dispersion in the primary direction (e.g., for the phase dispersion exemplified in Fig. 5.2, there would be 5 passes).

To validate the concept, we set out to design such space mapping antenna with initial goals of an operating range between 5.5 GHz and 6.5 GHz. The following sections outline the main considerations in the design process of the antenna, and presents measured results that are compared to simulation.

### 5.1.1 Feed Network Using Via-Less CRLH Stripline Unit Cell

Ideally a feed network should be implemented without affecting the radiation pattern of the radiating elements array. When utilizing a typical CRLH microstrip line for the feed network, the pattern interference can be difficult to avoid because of its natural continuous phase constant ( $\beta$ ) variation from negative to positive. This means that there is a fast wave ( $|v_p| > c$ ) region of operation and the line behaves like a uniform LWA radiating part of the energy [26]. We are interested in a varying phase constant without radiative effects. Lumped element based CRLH networks can be used but present a high operating frequency limit of around 4 GHz due to inherent self resonances. An enclosed distributed structure is then desired.

Radiation suppression, and avoidance of the loss associated with it, has historically been some of the advantages of striplines over microstrip technology TLs. A CRLH stripline is

proposed here for these benefits with a modified version of the via-less CRLH stripline first introduced in [28]. The via-less unit cell design was devised primarily to facilitate our fabrication effort. Our in-house capability to maintaining via position accuracy and guarantee via metal contact to the center conductor of a stripline was a significant concern.

As mentioned before, the feed network along the primary direction is preferred to be selected for the highly progressive phase TLs. The main reason for this is that there is only one progressive phase network in this direction. In the secondary direction, each linear array will need its own progressive phase network. Since a significantly larger area is needed to achieve greater phase progression (hence the meandering in a traditional serpentine approach), having only one of these large networks provides significant space savings over the multiple ones otherwise needed. The increase in size of the phase progression network in the secondary direction would also make it difficult to maintain the radiating elements at their optimal design intervals. In addition, the phase progression in the various linear arrays in the secondary direction have to match, which is more difficult to achieve with high progressive phase networks.

The modified CRLH stripline devised for this feed network is depicted in Fig. 5.3(b) with its stripline stackup detailed in Fig. 5.3(a). It is a compact folded version of the one in [28] capable of achieving more phase progression over the same distance. It offers both phase delay and advancement, seen in the dispersion diagram provided for reference in Fig. 5.3(c).

The diagram in Fig. 5.3(c) points to an unbalanced unit cell (there is a band gap between the left-hand and right-hand region, [14]) and is not evenly positioned over the intended operating frequency range (5.5 GHz - 6.5 GHz). The reason for this is that the diagram was obtained from a 3D EM eigenmode simulation of the geometry of only the final unit cell. Although the design process initiated with a balanced unit cell centered over the operating frequency range, additional tuning was needed once in the feed network environment seen in the final circuit in Fig. 5.6. The overall phase progression is a combination of the CRLH

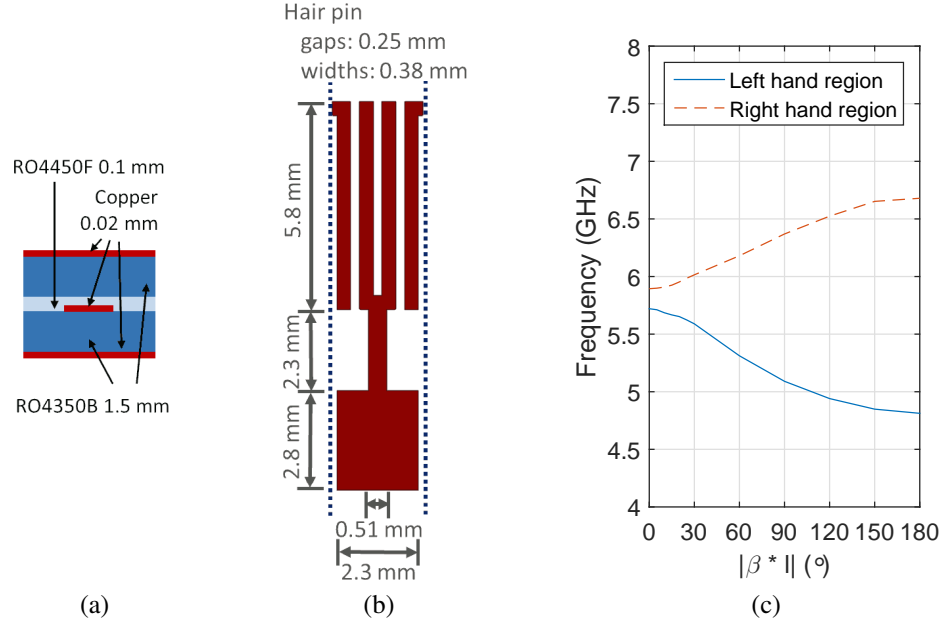


Figure 5.3: Compact (folded) via-less stripline unit cell used for feed network. (a) Stackup. (b) Geometry. (c) Dispersion. Length  $l = 2.54$  mm.

property of this unit cell with the right-hand TLs in between. That, as will be seen, is balanced and centered at about 6 GHz, and was fine tuned by adjusting unit cell dimensions while monitoring the return loss and progressive phase between output ports.

As the simulation models included an increasing amount of features, the simulation times became an issue since they would take very long to achieve the convergence desired. This is a common issue when simulating CRLH TLs because of the tight couplings in the models and the increase of the signal paths to multiple values of the wavelengths make it worse. To circumvent this issue the design time was reduced by approximating the stripline structure, as seen in Fig. 5.4(a), to a vertically symmetric structure, as seen in Fig. 5.4(b). The reduced model is constituted of only the top half of the stripline stackup with a perfect H boundary defined along the middle that also slices the center conductor in half. This perfect H boundary is equivalent to a *perfect magnetic conductor* [30], which enforces no magnetic field components tangential to the surface, as implied by the following expression:

$$\hat{n} \times \overline{H} = 0 \quad (5.1)$$

where  $\hat{n}$  is a unit vector in the direction normal to the surface, and  $\times$  represents the vector cross product operation. The perfect H boundary over the conductor strip region actually is internal to the strip where no fields exist since the solver considers the strip a perfect conductor internally.

The 3D modeler will then require a mesh of half the original size for an equivalent level of convergence. This, in turn, allows the 3D EM solver to analyze the model significantly faster. Results for models simulated both ways were compared and any discrepancy perceptible were at far lower power levels than required. It is interesting to note that it is not possible to reduce the model size in this same manner for a microstrip based CRLH TL because there is no such vertical symmetry.

By simplifying the 3D model with the perfect H boundary condition mentioned, the whole feed network could be simulated. The final full feed network model can be seen in

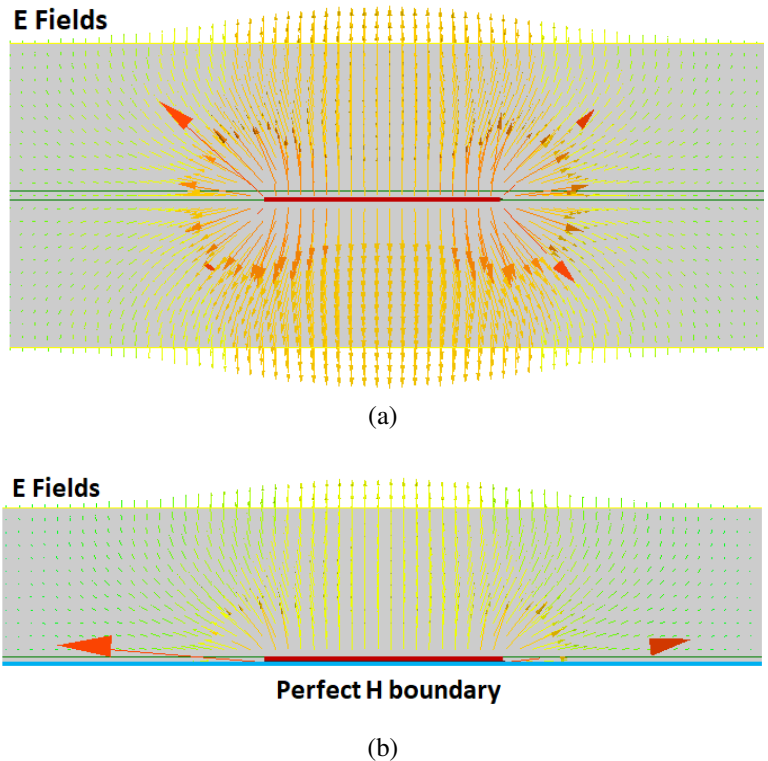


Figure 5.4: Electric fields on a vertical cross section of a stripline in this stackup. (a) Full stripline model. (b) Stripline model using a perfect H boundary condition along the vertical center.

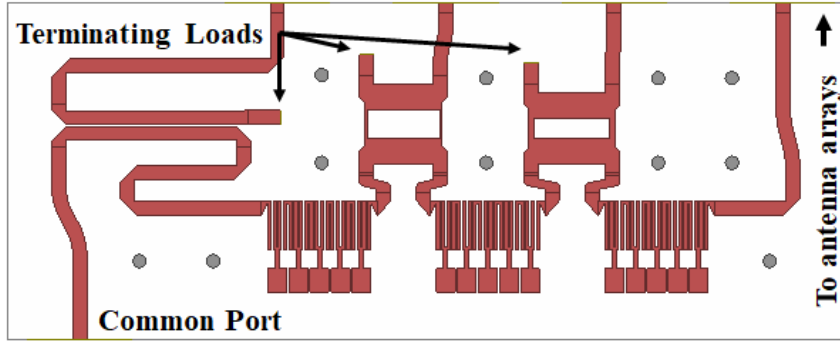


Figure 5.5: Top view of full feed network model in which perfect H boundary condition was used.

Fig. 5.5. In it, the isolated port of all couplers are terminated with  $50\Omega$ . Also, vias that extend from top ground to bottom ground of the stripline can be seen in a few locations of the model. This is because in stripline there is the opportunity for higher order waveguide modes to be excited. Placing mode suppression vias is a common practice in stripline design to ensure fundamental mode operation of circuits.

The fabricated circuit in Fig. 5.6 shows that with the new folded unit cell size, it is possible to fit 8 cells in a distance shorter than  $\lambda/2$  at highest frequency of 7 GHz, avoiding early onset of grating lobes [18]. This amount of unit cells is sufficient to provide a progressive output phase of  $+360^\circ$  to  $-360^\circ$  which is sufficient for our concept validation purposes.

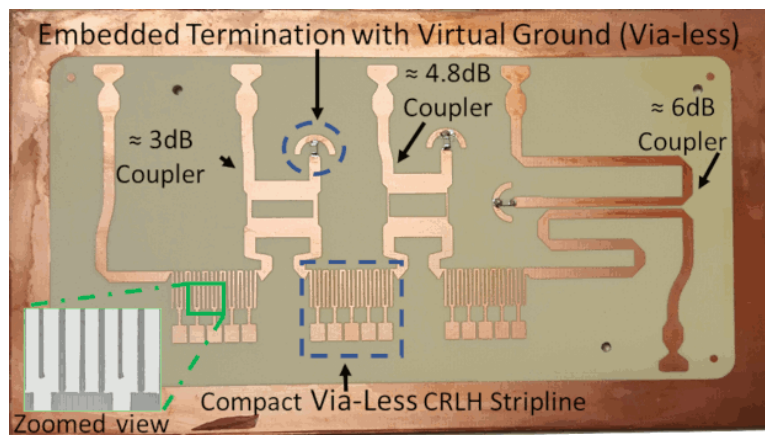


Figure 5.6: Feed network bottom board prior to lamination.

To provide a sense of the area reduction opportunity that the CRLH stripline can offer, a traditional serpentine network was simulated to provide the same phase progression over the operating band. For the same stripline stackup the reduction of required area, for a single progressive phase section, was approximately 5x. This can be seen in the overlay of the two cases provided in Fig. 5.7. The overall feed network reduction is obviously less than that, but, in a real application a significantly higher progressive phase network would likely be required, making the overall reduction in such case significant. Some slight disadvantages of CRLH stripline compared to traditional stripline is degraded insertion loss (simulated average increase in loss of 13%) and return loss but these can be acceptable given the opportunity for size reduction.

Several power division circuits were investigated for this application (including simple line splits and Wilkinson power dividers), and ultimately branchline couplers and a coupled-line directional coupler were selected to achieve a uniform taper. Branchline couplers were used for moderate power split ratios and by tuning lengths / widths it was possible to achieve non-symmetrical power ratios over the operating band to better compensate increased loss of the CRLH TL at the higher frequencies. A coupled-line directional coupler was used for the high power split ratio necessary at the first tapping point and, as an atypical case, the coupled length used was  $3/4\lambda$ . The reason for this is that a single  $\lambda/4$  directional coupler provides a  $90^\circ$  phase advance to the low output power port, whereas a  $3/4\lambda$  directional coupler provides a  $90^\circ$  delay which matches the delay of the branchline couplers used at the subsequent tapping points.

A stripline termination was designed for the isolated port of all couplers (visible in

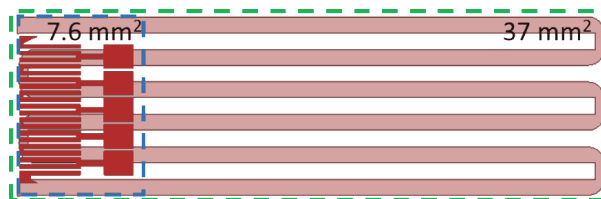
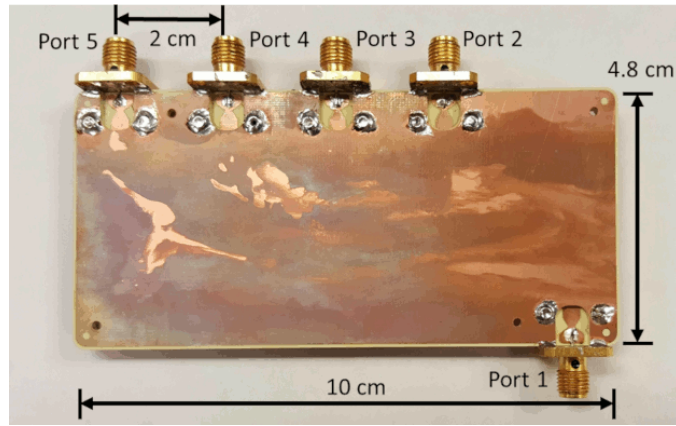
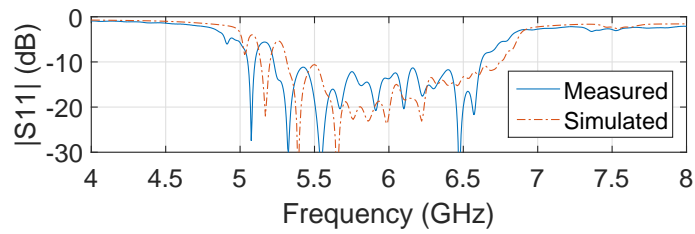


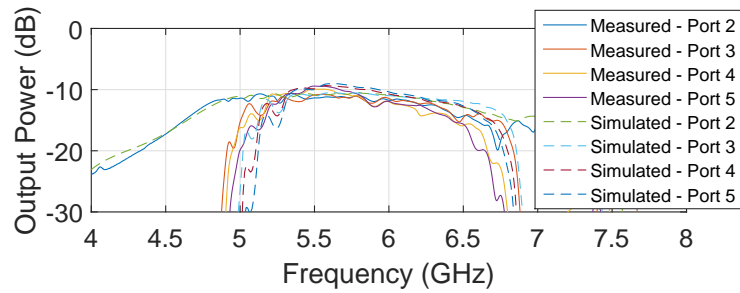
Figure 5.7: Via-less CRLH stripline versus traditional stripline area comparison.



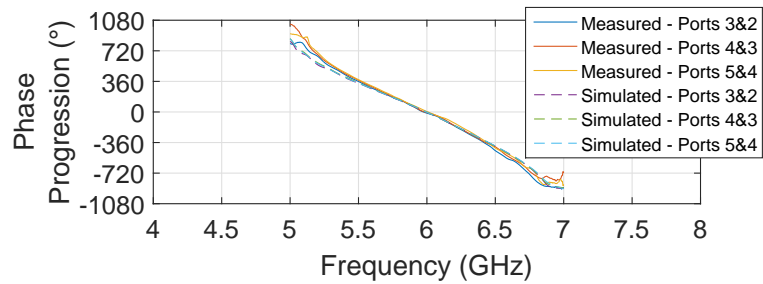
(a)



(b)



(c)



(d)

Figure 5.8: Feed network test board. (a) Test board. (b) Return loss performance. (c) Output power. (d) Output phase progression.

Fig. 5.6). It makes use of a resistor embedded into a cavity for integration purposes, and to maintain the via-less concept, a virtual ground over operating frequency was achieved at

the pad of the resistor through impedance transformation of an open stub.

A well performing prototype (Fig. 5.8(a)) was built and a comparison between simulated and measured return loss, phase progression and amplitude taper is depicted on Figs. 5.8(b), 5.8(d), and 5.8(c), respectively. Note that the good return loss and  $0^\circ$  progressive phase around 6 GHz suggests that the combination of CRLH and RH TLs is balanced, unlike the CRLH by itself as previously pointed out. All fabrication steps, including photomask generation, resist coating, exposure, wet etching, drilling, and bonding, took place at our facilities and several fabrication iterations were necessary to achieve consistent line widths. It is important to note that initial iterations presented a bandgap, between the left and right-handed frequency bands, due to variations on the narrow line widths throughout the board. This bandgap was evident in the degraded return loss performance around the center frequency.

Based on the output power measurements shown in Fig. 5.8(c), the dissipation loss of the feed network has been calculated to be on average 4.9 dB in the operating band which is close to simulation prediction. The affect of this loss in the system efficiency will be discussed at the system level.

### 5.1.2 Linear Antenna Arrays

The antennas in the array can be chosen from many types of antennas available and the selection often will be made based on factors such as desired polarization, footprint and cost of implementation. For many of these cases the phase progression along the linear arrays direction can be provided by a CRLH stripline (like the one described in the previous section), with tapping points along it leading to the radiating antenna elements, potentially on a separate layer. As mentioned, open CRLH TLs have a natural capability of radiating energy as waves propagate through them. With proper design, CRLH LWAs can provide phase characteristics for backward to forward scanning, occupying less space. To emphasize the use of CRLH TLs in frequency scanning applications this is the approach chosen

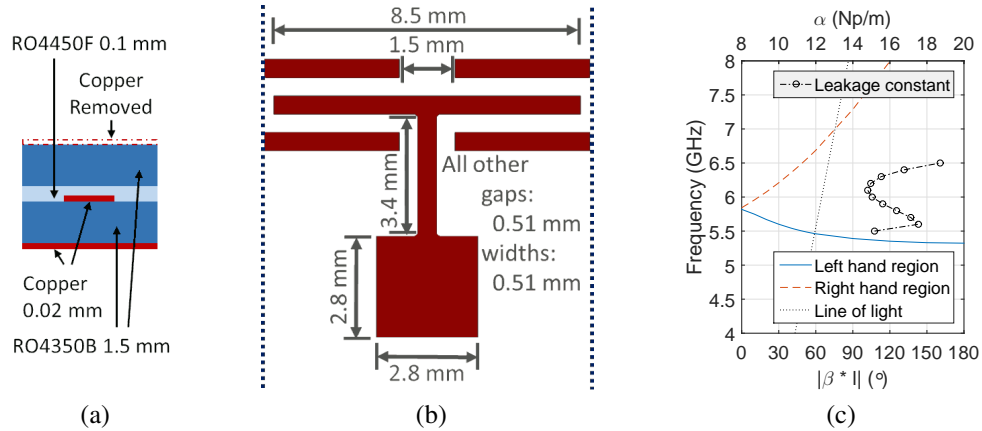


Figure 5.9: Via-less CRLH loaded microstrip line unit cell used for LWA. (a) Stackup. (b) Geometry. (c) Dispersion and leakage constant. Length  $l = 9$  mm.

for our antenna.

CRLH LWAs using microstrip lines or substrate integrated waveguides can be used with the proper transition. The technology chosen here, however, was the loaded microstrip lines. This stackup is achieved by simply removing the top copper from what would otherwise be a stripline. This approach allows us to conceal and protect the array structure in an elegant way. It eliminates some requirements of a typical microstrip line antenna, such as the need for a radome and plating/passivation of the exposed copper of the antenna elements. Vias have been used to transition the top ground currents from the stripline to the bottom ground of the loaded microstrip lines. Note that the design does include grounding vias (in some cases for mode suppression) but they do not connect to the center conductor layer and positioning errors do not affect performance significantly.

The designed LWA unit cell can be seen in Fig. 5.9(b) and is the same type reported

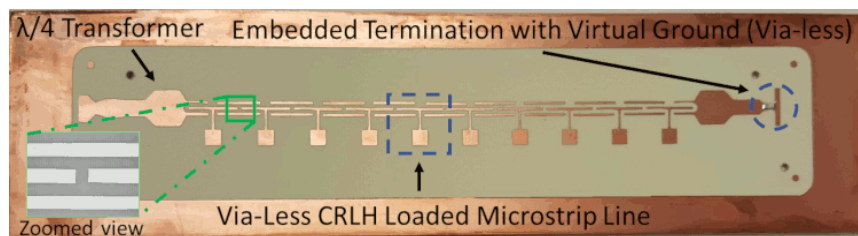
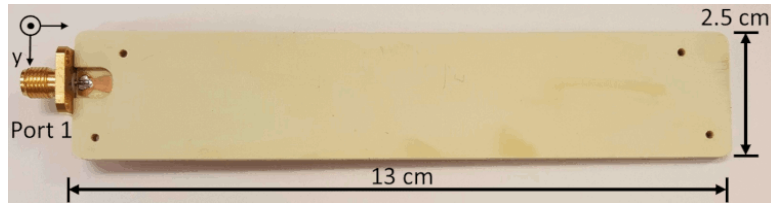


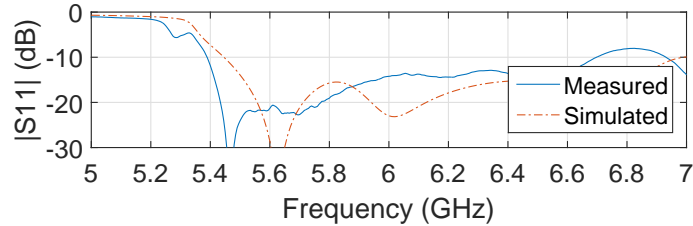
Figure 5.10: Leaky wave antenna bottom board prior to lamination.

in [28] with the exception of the stackup here being a loaded microstrip line(see Fig. 5.9(a)). It has been tuned through 3D EM eigenmode simulations to provide the dispersion characteristics displayed in Fig. 5.9(c). The length of the unit cell and dispersion provided are key aspects to be tuned. As previously mentioned, only a single scanning sweep is desired in this direction. If we consider each unit cell as a radiating element with distance between elements equivalent to the cell length, one can use the calculated dispersion characteristics to roughly predict scanning capability based on antenna array theory [18]. Due to the stackup selection and characteristics of the cell type chosen, the characteristic impedance of the cell during tuning had a slight mismatch to that of the system. This would then be easily mitigated through the use of impedance transformers. Once an acceptable pair of unit cell length and dispersion characteristic was achieved, a 3D EM simulation of the linear LWA was set up to verify scanning performance. The number of unit cells in the linear array can be made large for pencil beam applications. Here 10 unit cells were chosen so that the effective aperture along its direction would roughly match that of the other direction (or roughly the same beam width in both directions).

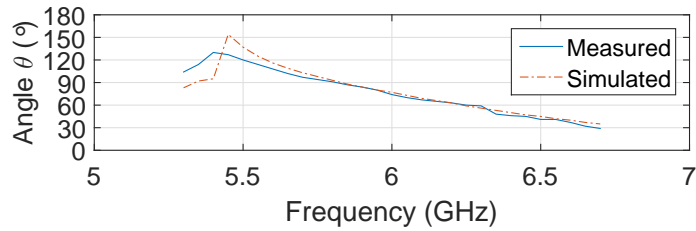
The final LWA layout is visible from the bottom laminate depicted in Fig. 5.10 in which it can be seen that  $\lambda/4$  impedance transformers and embedded termination with virtual ground have been used. A few iterations of test boards (Fig. 5.11(a)) were built until an etch compensation was settled on. It is worth noting that there were less issues associated with etching since the gaps and line widths for this part were not as narrow as in the feed network. Measurement results roughly matched simulated predictions, as seen in the return loss in Fig. 5.11(b) and scanning angle in Fig. 5.11(c). The scanning angle was determined by the direction of beam peak at each frequency. The left-handed region ( $\theta > 90^\circ$ ) differs slightly from simulation in both measurements and is attributed primarily to etching irregularities since the circuit line widths and gaps for all iterations of this board had been measured prior to bonding and minor variations from the simulated quantities were always present.



(a)



(b)



(c)

Figure 5.11: Leaky wave antenna test board. (a) Test board. (b) Return loss performance. (c) Scanning angle of leaky wave antenna.

## 5.2 Measurements of an Integrated Array

Since predicted performance of feed network and LWA test boards was validated, the circuits were then integrated into a single layout (see Fig. 5.12(a)). The radiating portion, that is, the 2D LWA array, was analyzed in its entirety through 3D EM simulation taking into account the mutual coupling between the neighboring linear arrays, as seen in the model in Fig. 5.13. In this case the spacing between the linear arrays was sufficient to not impact return loss significantly, and the simulated radiated beams were deemed acceptable. These results, along with those already available from the feed network model, were joined in circuit simulator for full antenna performance prediction. A single 3D EM model would have been troublesome to simulate due to memory requirements. The fact that we have an enclosed (non-radiating) feed network lends well to this simulation by parts approach.

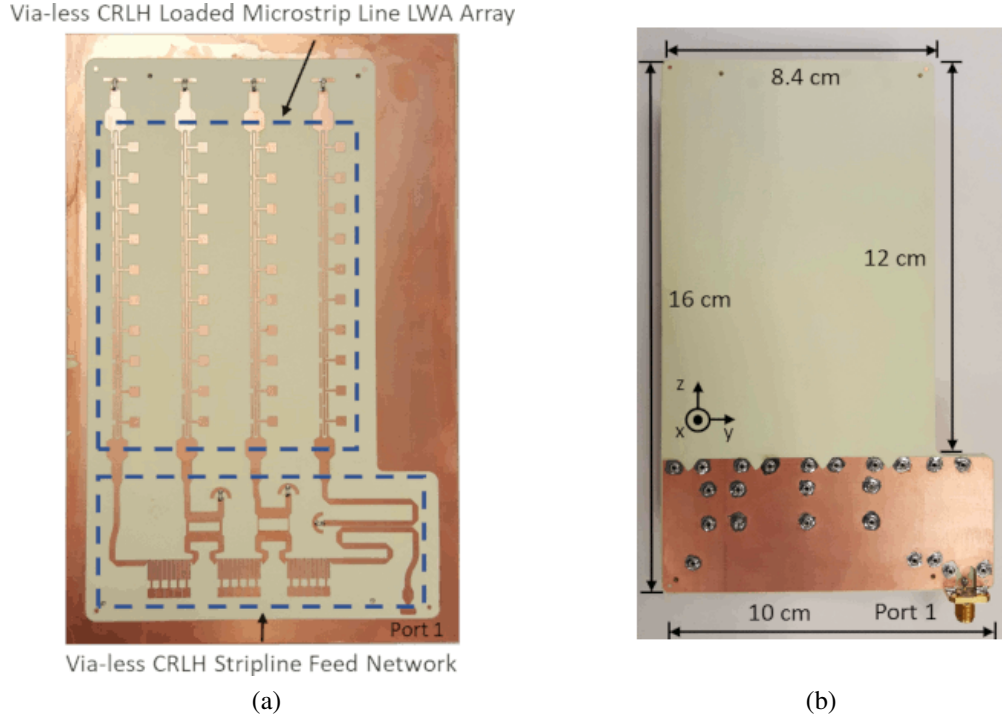


Figure 5.12: Integrated prototype. (a) Bottom board. (b) Prototype.

A single final fabricated board, seen in Fig. 5.12(b), was initially tested by measuring the return loss of its single port. The response, as seen in Fig. 5.14(a), shows a degradation between 5.75 GHz and 6.1 GHz, with good return loss (better than 10 dB) before and after. This is very much alike the response observed in some of the feed network test boards in which the line widths/gaps of their CRLH stripline were different than intended thus detuning the balanced frequency of 6 GHz. This detuning starts to introduce a bandgap region between the lower frequencies (left-handed region) and the higher frequencies (right-handed region). In this case the signal is still able to pass through, so performing multiple fabrication iterations to completely remove these minor bandgap effects was avoided. As was the case with both the feed network and LWA test boards, the use of better compensation factors and better control of the etching processes would improve the correlation with simulation.

Since the source of return loss degradation is understood, we proceeded to characterize the radiation patterns over the operating frequency range. Measurements were taken of

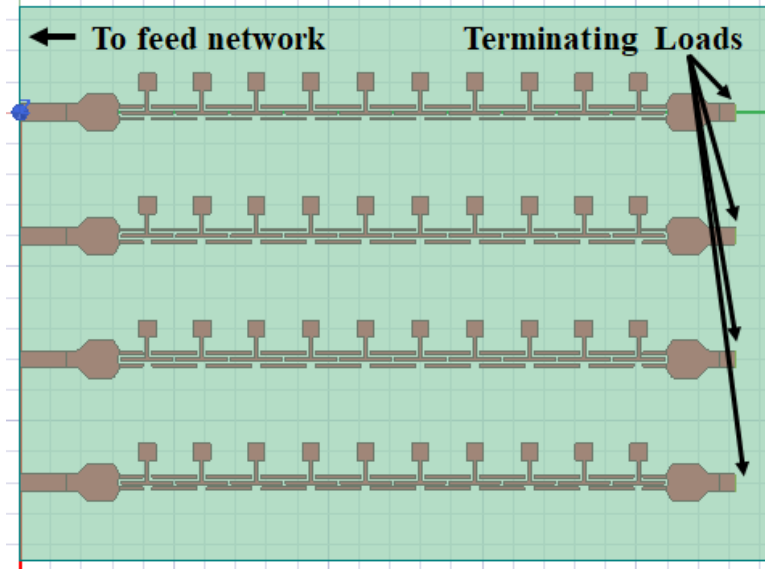


Figure 5.13: Top view of full antenna array model.

the total radiated power in the radiating hemisphere ( $-90^\circ < \phi < 90^\circ$ ,  $0^\circ < \theta < 180^\circ$ ). The patterns were measured with  $5^\circ$  step for a reduced data acquisition time, and, to better assess the frequency scanning capability, a frequency interval of 10 MHz was used, with measurements from 5.28 GHz to 6.72 GHz.

The measured patterns were processed in MATLAB to provide an animation of the beam steering as excitation frequency increases from lowest to highest. A smooth scanning capability was observed throughout most of the test points and a representation of this is shown through snapshots available in Fig. 5.14(b). Distortions to the beam were observed at the very beginning and end of the band, and at the narrow scanning row transitions, as expected. At the row transitions, as the beam is ending a scanning sweep and approaches the board plane, the new beam starts to rise at the opposing direction and spurious beams are observed in between, as a result of the array factor.

By means of cubic surface interpolation [46], the beam peaks were determined on a  $1^\circ$  grid (from the  $5^\circ$  grid data). By plotting the beam peaks on a chart representing the hemisphere coordinates, the scanning route of the beam can be better understood. Fig. 5.14(c) depicts this information and it can be seen that the beam sweeps 3 times over. These results

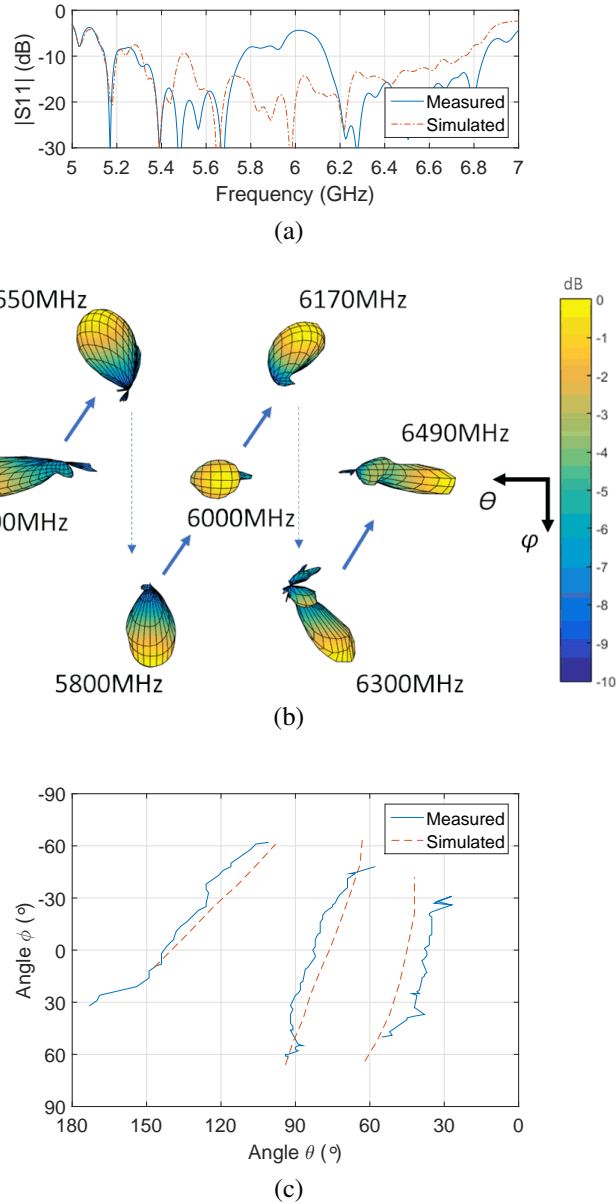


Figure 5.14: Measurement results of the integrated prototype. (a) Return loss performance. (b) Sample of measured radiation patterns (normalized). (c) Scanning route (beam peak position as frequency is swept).

are in line with expectation from simulation. The design was for roughly 2 sweeps (half, full, and half), however, this chart shows data points out of the initial intended frequency range. The data points near the narrowband row transitions were omitted for better visualization of the useful range. In an application, signals measured in these ranges may need to be ignored. These results validate the beam steering capability and the potential for use in

Table 5.1: Integrated Array Radiation Characteristics

Frequency	Simulated						Measured				
	$\theta$	$\phi$	$\theta$ BW	$\phi$ BW	Directivity	System Radiation Gain	$\theta$	$\phi$	$\theta$ BW	$\phi$ BW	Directivity
5450 MHz	147°	10°	36°	39°	10.7 dBi	6.3 dBi	144°	5°	36°	31°	11.9 dBi
5550 MHz	123°	-25°	39°	42°	12.4 dBi	7.1 dBi	129°	-23°	46°	41°	11.5 dBi
5700 MHz	98°	-61°	29°	49°	11.6 dBi	5.7 dBi	106°	-61°	32°	44°	10.8 dBi
5750 MHz	94°	66°	27°	50°	10.6 dBi	4.3 dBi	94°	60°	31°	24°	12.3 dBi
5850 MHz	87°	40°	30°	38°	14.1 dBi	8.7 dBi	91°	45°	32°	34°	13.4 dBi
6000 MHz	76°	-1°	30°	31°	14.8 dBi	9.3 dBi	8°	24°	34°	32°	13.0 dBi
6100 MHz	68°	-32°	31°	37°	14.4 dBi	8.5 dBi	80°	-16°	28°	29°	13.4 dBi
6200 MHz	63°	-64°	25°	53°	12.5 dBi	5.2 dBi	69°	-40°	37°	33°	10.4 dBi
6350 MHz	52°	37°	33°	45°	14.2 dBi	7.5 dBi	45°	39°	36°	32°	10.1 dBi
6400 MHz	48°	19°	39°	41°	14.3 dBi	7.5 dBi	43°	25°	33°	30°	10.7 dBi
6500 MHz	42°	-21°	38°	45°	14.5 dBi	7.1 dBi	38°	5°	36°	25°	10.6 dBi

imaging and radar applications.

Additional radiation details of a select amount of frequency points of Fig. 5.14(c) is available in Table 5.1. It includes simulated and measured beam peak positions, beam widths (BWs), and directivity. Simulated system level radiation gain, which includes the loss of the feed network and 2D LWA array, is also presented. Unfortunately a standard gain horn antenna covering this frequency range was not available so actual measurements of gain are not provided. When considering the  $\theta$  and  $\phi$  beam widths, it is seen that they are roughly the same at broadside (around 6 GHz), which was a goal previously mentioned. As the frequency varies there are competing phenomenas affecting the changes to beam widths as well as gain. Based on antenna array theory it is expected that with the increase in frequency the beam widths will become narrower, due to the increase of the aperture to wavelength ratio, increasing the directivity and, thus, the gain. However, this is not clearly observed here since the beam direction changes as well. For frequencies for which the beams are closer to the array plane, the array factor yields wider beam widths due to the decreased effective aperture when considering the array projection onto the plane perpendicular to the beam. This also results in lower directivity and gain. This dominant effect can be seen in the simulated results around 5.75 GHz and 6.2 GHz. This variation is not ob-

vious, however, in the measurement results. It is assumed that fabrication inaccuracies are the reason for this. When considering simulated gain and directivity, the system radiation efficiency is calculated to be about 25%. This is driven primarily by the dissipation loss of the feed network. As previously mentioned, the loss of the CRLH TLs used in the feed network is comparable to that of the traditional meandered approach in the same stackup. This is an area for improvement through selection of low loss materials or, potentially, different types of stripline CRLH structures.

It is worth noting that the scanning region should be expected to be in practice less than the full hemisphere, as is observable in Fig. 5.14(c). This is due to the fact that the effective radiation pattern is given by the combination of the array factor and the individual radiating element pattern. In this case the element radiates poorly below  $30^\circ$  from the array plane, setting, therefore, the bounds of the scanning region.

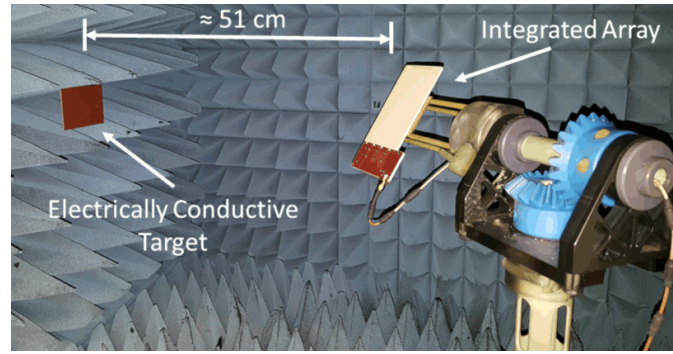
### **5.3 Radar Application Test**

The good beam steering capability allowed us to consider an end use scenario. Given our measurement capabilities, we decided to test the antenna in a limited radar application. The goal was to detect a reflective target at a few pre-established locations.

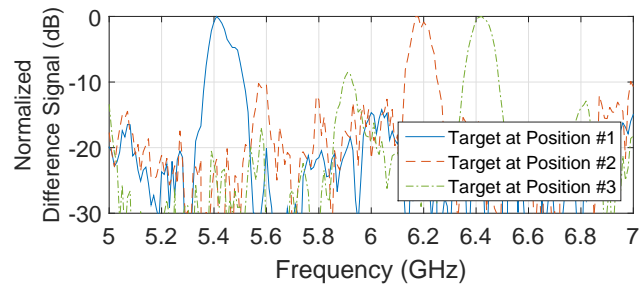
The simple technique adopted for this experiment was to utilize the transmit/receive capabilities of a network analyzer connected to the antenna in the anechoic chamber. By measuring the return loss over the operating frequency of the prototype, targets should be detectable by reflected signals at the frequencies of the beams in the direction of the target.

The prototype was oriented such that the radiating hemisphere pointed away from the chamber's probe as it is not used and would introduce undesired reflections. The target utilized was a roughly 8 cm square piece of copper cladded laminate placed at a 51 cm distance from the prototype, as seen in Fig. 5.15(a). The prototype was then rotated to three specific orientations with return loss sweep measurements taken.

The target reflected signal, although present, was saturated by the return loss of the pro-



(a)



(b)

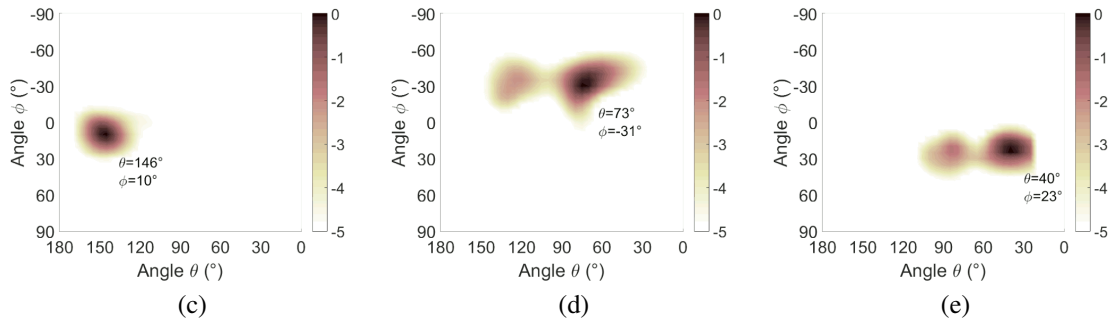


Figure 5.15: Radar application measurement results. Target detection within  $5^\circ$  cone of intended position. (a) Measurement setup for target detection. (b) Detected signals. (c) Target at position #1. (d) Target at position #2. (e) Target at position #3.

tototype itself. In order to focus on the reflected signals of the environment, rather than that of the antenna, baseline return loss measurements were taken at each orientation without the target present and used as reference. The reference was then subtracted from the target detection measurements and the result is a modified reflection signal in which the reflected target signals have been extracted, as shown in Fig. 5.15(b).

The direction of the target in this experiment could be determined by relating the peak signal(s) with the known beam peaks previously characterized by the radiation patterns.

Table 5.2: Radar Target Positions

Position	Intended		Detected	
	$\theta$	$\phi$	$\theta$	$\phi$
#1	150°	10°	146°	10°
#2	70°	-35°	73°	-31°
#3	45°	25°	40°	23°

To obtain a radar image, however, we multiplied the series of radiation patterns by the modified reflection signal, in essence using the detected reflection at the various frequencies as weights.

Using the method described, we were able to detect the position of the three target cases. A list of the intended target positions as well as the positions that were detected is available in Table 5.2. The radar images generated can be seen in Figs. 5.15(c), 5.15(d), and 5.15(e). The detected angular positions were within a 5° range from the intended positions. This is well within expectations given uncertainties in the prototype and target positions, the angular resolution of the radiation patterns used, and considering that the target has an angular width of about 8.6°.

The regions in Figs. 5.15(d) and 5.15(e) which look like secondary targets are primarily due to sidelobe levels. To improve the image, narrower beamwidths and lower sidelobe levels are needed overall. This is attained by a larger array effective aperture (size), use of amplitude tapers and better control of amplitudes and phases through tuning and processes control.

To extract the range information out of the reflected signal, other well known radar techniques can be used as discussed in [47] and [37]. The delay between the transmitted and reflected signals can be quantified to estimate the distance to the target based on the devices delay and the free space propagation velocity. With this standard radar implementation a true 3D detection can be accomplished.

There are several aspects to consider when utilizing a 2D frequency scanning antenna

array, like the one used here, for radar applications. These are related to the nature of frequency scanning and are not unique to this CRLH stripline implementation. One aspect is in regards to the angular resolution. Since each scanning row relates to a sub-band of the overall operating frequency band of the antenna, the increase of scanning rows increases the number of sub-bands which results in a reduction of bandwidth of each individual sub-band. Although the row of a particular sub-band is still scanned in its entirety, the angular position of the beam varies faster with the change of frequency, that is  $\frac{d\theta_{beam}(f)}{df}$  is larger and a higher degree of resolution is needed in the frequency detection for the same level of angular resolution in the scanning row. A basic method to determine the angular position from frequency scanning antennas is by binning the return signal by frequency through the use of a filter bank composed of *matched filters* [17] [48] followed by power detector circuitry. An increase in the number of scanning rows would increase the quantity of filters and associated circuitry, but also would increase the complexity of the filters since they would need to filter narrower frequency bands. This is less of an issue if the response is processed digitally through the use of Analog to Digital converters.

Another aspect to consider is in regards to the range resolution and discrimination. For a basic radar system transmitting a sinusoidal signal there is a determined resolution. The range discrimination, which is the ability to discern between two or more targets, is known to be poor because two targets near each other will reflect the signal at a slightly different time but with the same frequency. Depending on the duration of the transmitted signal these reflected signals overlap in time and it is not possible to discern between the two targets. Typical radars use transmission *pulses* (signals of short duration) which, among other benefits, help reduce reflected signal overlaps. The use of a linear frequency modulated signal as the transmission signal, such as the *chirp* [17] waveform, also mitigates the overlap issue of the reflected signal because although the reflected signals of the targets may overlap, at the time that they do overlap they will be of different frequencies. Frequency scanning radars typically already use a form of linear frequency modulated signal for scan-

ning. In the case of a 2D frequency scanning radar, as discussed in the previous paragraph, the angular position varies faster with frequency within a scanning row which means that the bandwidth that covers a target in space is even smaller, effectively limiting the range resolution. The use of a technique called *pulse compression* can be used to further improve the resolution [48]. The technique makes use of a *compression filter* circuit [49] [50] whose purpose is to delay the frequency components of the reflected signal in a manner inversely proportionate to the frequency. Since the frequency of the reflected signal of a target will start with a lower frequency and increase as time passes, the effect of the compression filter is to delay the beginning of the reflected signal, compressing the reflected pulse in time. This allows the receiver of a frequency scanning radar to increase range resolution and discrimination capability [51].

#### **5.4 Traditional CRLH Stripline Implementation**

The folded unit cell used in the feed network portion of the array, which had as primary function to provide high phase progression of the traveling wave, provided significant reduction in size when compared to the traditional meandered stripline approach. This was achieved with a unit cell comparable in size to the wavelength and it is straightforward to conclude that a smaller unit cell would provide opportunity for an even greater compression ratio of the feed network circuit.

Traditional CRLH unit cells which can be reduced to lumped  $L_R$ ,  $C_L$ ,  $C_R$ , and  $L_L$ , as in Fig. 2.2, have, in other transmission structures, such as in microstrip and substrate integrated waveguides, been able to achieve unit cell sizes quite smaller than the wavelength. In a stripline structure, the use of plated-through-holes (in reference to the *plating* process [52] of depositing a thin metal coat over a conductor) is capable of providing the inductance to ground necessary for the traditional unit cell approach and could potentially lead to a smaller unit cell than the one used in the prototype. The feed network structure would then require industry standard methods for plating drilled holes with reliable con-

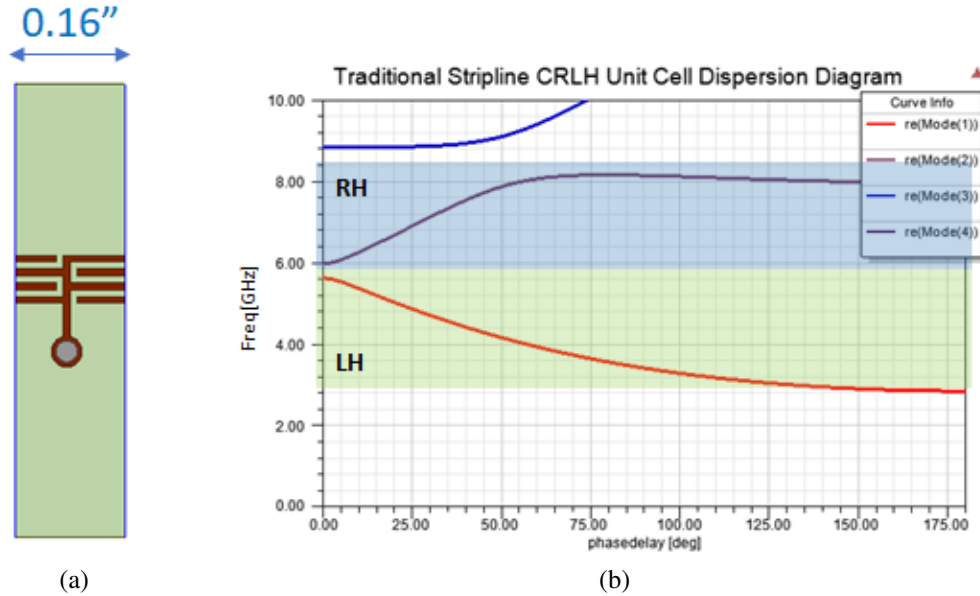
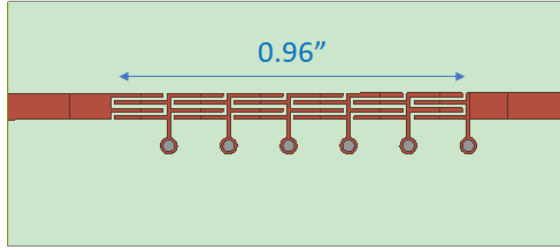


Figure 5.16: Traditional CRLH stripline unit cell in the same stackup tuned for balanced frequency of 6 GHz. (a) Top view of 3D Model. (b) Dispersion diagram.

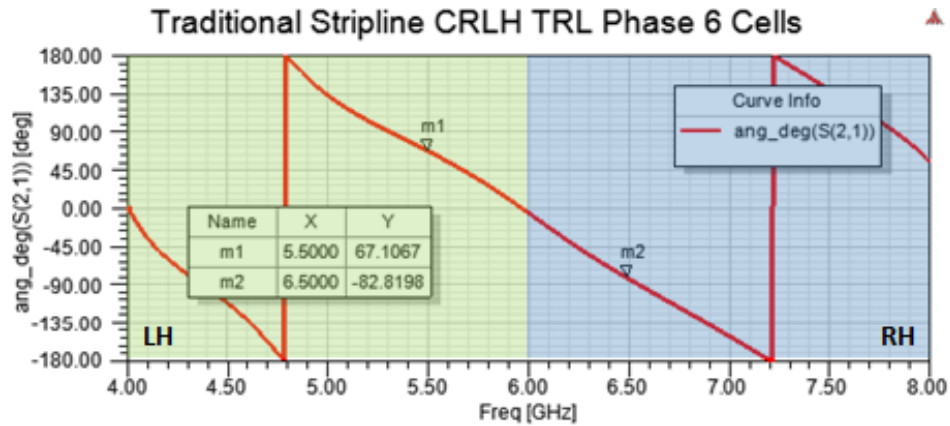
nections to the conductors in the center layer. Nevertheless, the traditional unit cell has been investigated from a simulation perspective in an attempt to identify a unit cell that would yield a smaller feed network for the same application.

For equivalency, as has been done with the comparison to the traditional stripline meandered line case, the same stackup (Fig. 5.3(a)) has been considered as in the previous cases. The unit cell is composed of a series digital capacitor with a shorted stub to ground, as in Fig. 2.3. The dispersion characteristics was tuned again via EM eigenmode solver by adjusting parameters such as number, width and length of fingers of the interdigital capacitor, the gap between them, and the width and lengths of the shorted stub. The goal was to arrive at a unit cell model with balanced frequency of 6 GHz.

The tuned unit cell can be seen in Fig. 5.16(a) along with its dispersion characteristics in Fig. 5.16(b). There are two aspects that negatively affect the choice of this unit cell when in comparison to the folded via-less unit cell. The first aspect is that this unit cell length, in the direction of the feed network, is 0.16" versus the 0.1" length of the folded unit cell in Fig. 5.3(b). This means that without meandering a smaller number of unit cells



(a)



(b)

Figure 5.17: Six traditional CRLH stripline unit cells cascaded. (a) Top view of 3D Model. (b) Phase progression of cascaded model.

can be placed in between the linear antenna arrays. The second aspect is that although both cases have the balanced frequency of 6 GHz, this unit cell does not have as steep of dispersion: the phase through the folded via-less unit cell varies from  $-180^\circ$  to  $-180^\circ$  in a 1.4 GHz span (see Fig. 5.3(c)) where as this traditional unit cell needs a 5 GHz span for the same phase variation. This means that either more bandwidth is needed to scan over same angular space (under the assumption that all else is the same) or that more unit cells are needed to maintain same spatial coverage over the same bandwidth. To better understand this, consider the cascaded model of six of these unit cells depicted in Fig. 5.17(a). This spans a longer length than that used between the linear antenna arrays in Fig. 5.6. Yet, as seen in Fig. 5.17(b), the overall phase span from 5.5 to 6.5 GHz is roughly  $150^\circ$ , where as for the folded via-less case, over the same frequency range the phase span is  $> 720^\circ$  as seen in Fig. 5.8(d).

There are a few ways that may address the issues encountered but these require important changes in the stackup which destroys the equivalency attempt. For the cell length, the interdigital capacitor can be substituted by a parallel plates capacitor. A higher series capacitance could then be attained in a smaller length, but at the cost of needing a more complex stripline with center board construction to separate the plates. To narrow the overall dispersion span, there are indications that either reducing the ground plane spacing or increasing the permittivity of the substrates would achieve this effect.

Based on these findings, although the traditional unit cell could be used for feed networks with high phase progression, the folded via-less options is preferred. It could, however, be a good choice for the feed network of a single linear antenna array as was the case in Chapter 4. In that case the unfolded via-less unit cell measured significantly longer at 0.355" (Fig. 4.1(c)).

## 5.5 Summary

The goal of achieving a full hemisphere space to frequency mapping antenna array with CRLH TLs that can be extended for use in imaging and radar applications has been accomplished. Key aspects of this particular design include: the use of a via-less CRLH stripline for the feed network which prevents radiation leakage affecting radiation patterns, and a smaller footprint compared to meandered line approach; a construction that is not sensitive to via position; a CRLH LWA array that incorporates feed network capability with backward to forward radiation capability; and an integrated stripline/loaded microstrip line assembly for simplicity.

Feed network and LWA array portions of the design were tested prior to integration and the final integrated prototype performed within expectations given our manufacturing capability. The applicability of the antenna as part of a simple radar frontend was verified in a controlled environment with successful detection of a single target at various positions.

The results not only show a successful use of a via-less CRLH stripline in a feed net-

work application but also show that by using CRLH TLs in the design of 2D frequency scanning arrays, the size of the progressive phase portion of the network can be greatly reduced when compared to traditional meandering approaches. The amount of overall size reduction depends on the amount of phase progression needed for the application, that is, the number of scanning lines.

## CHAPTER 6

### WIDEBAND PHASE SHIFTER ELEMENT

In order to form arbitrary radiation pattern beams with electrically steered antenna arrays, a significant amount of control of the amplitude and phase is necessary. In antenna array theory, the expression for antenna array factor (as described in [18]) relates amplitudes and phases of every radiating element, with a radiated far field value that is a function of angular coordinates.

Amplitudes of signals are usually manipulated by use of unequal split power division to the antenna elements. Amplitude attenuators are also used at times, with the caveat of increase overall system loss and creating sources of heat due to the power dissipation. For phase manipulation, a simple approach is the use of regular transmission lines. Since the phase of the traveling signal changes as it propagates through the line, it is possible to achieve arbitrary phase values at the antenna elements at a given frequency by adjusting the length of transmission lines that lead to them. One significant drawback of this simple approach is that it is narrowband as at frequencies other than that specific frequency, the phase may drift differently for the various paths and dispersion can be observed.

Phase shifters are microwave circuit features that have the capability to present a phase offset that can better match dispersive paths, effectively increasing the bandwidth over which a fixed phase relationship can be maintained. CRLH TL unit cells, with their dispersion manipulation capability, are good candidates for use as phase shifters. Lumped element CRLH unit cells have been shown [53] to provide wideband  $90^\circ$  phase shifts for application in wideband circularly polarized antennas. In [53] the array consisted of four antenna elements, and each needed to be excited with a wideband phase offset of  $0^\circ$ ,  $90^\circ$ ,  $180^\circ$  and  $270^\circ$  in order to achieve the wideband circular polarization of the array. To achieve the various offsets, cascaded unit cells were used (see Fig. 6.1).

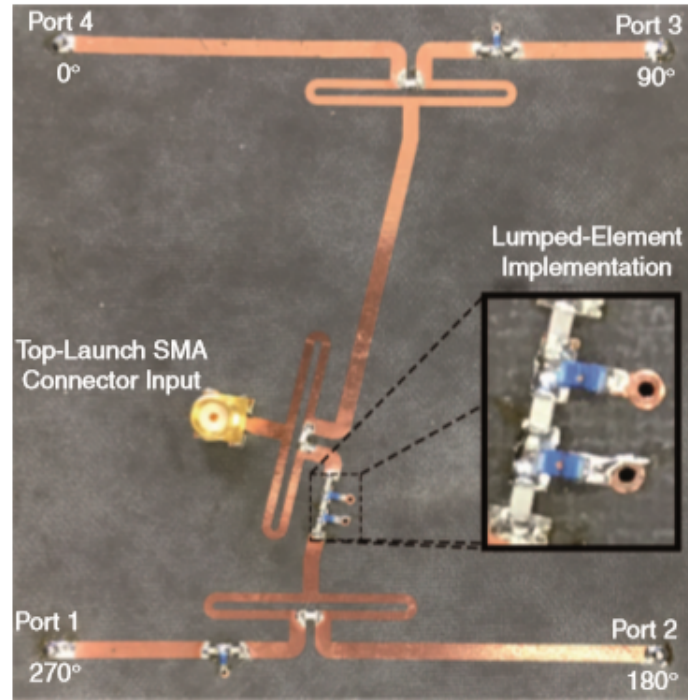


**Figure 9.** The one-to-four power-divider circuit prototype providing  $0^\circ$ – $90^\circ$ – $180^\circ$ – $270^\circ$  outputs using CRLH-TLs. SMA: subminiature version A.

Figure 6.1: Feed network for wideband circularly polarized antenna using lumped element CRLH TL for phase shifting. Figure reproduced from [53].

There are various non-CRLH methods of achieving this sort of phase shift. These methods in general make use of circuits with combinations of open or shorted stubs, such as referenced in the summary in [54] and seen in Fig. 6.2(a). The Schiffman phase shifter [55] is a well known method to achieve the linear phase offset through the use of coupled lines. All these methods are comparable in size to the wavelength as they make use of quarter wave transformers. Regarding distributed CRLH, the work presented in [56] illustrates the concept of using a microstrip CRLH TL to achieve a  $90^\circ$  phase offset. This structure, seen in Fig. 6.2(b), is compared to the Schiffman approach as occupying significantly less space. The microstrip line is exposed to air and is capable of radiating. If the side of the board where the phase shifting occurs is the same side as the antenna elements, there is the potential to deform the intended radiation pattern.

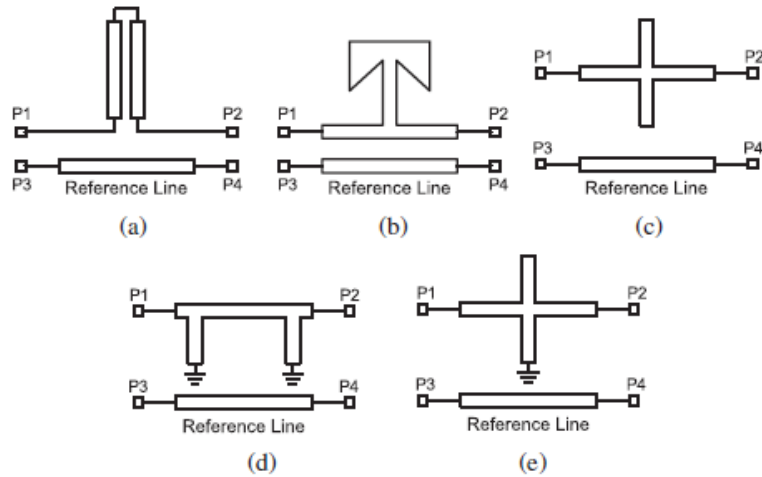


Fig. 1. Different topologies of phase shifters : (a) Schiffman [1] (b) T-shaped (open) stub [5] (c) open-open-stub [6] (d) short-short-stub [7] and (e) open-short-stub [8].

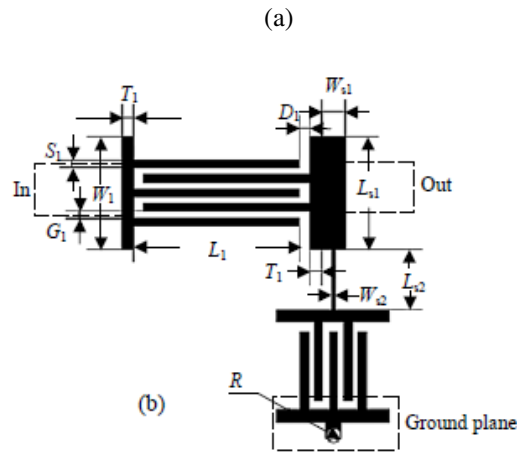


Fig.2 (b) The CRLH structure implemented on quasi-lumped elements

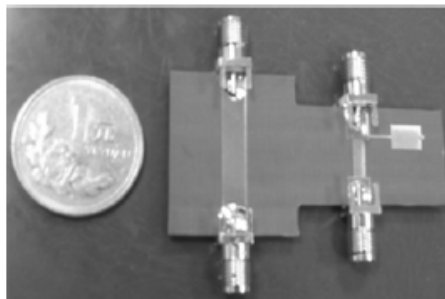


Fig.4 The fabricated device of the proposed differential phase shifter

(b)

Figure 6.2: Some examples of existent phase shifter options. (a) Various non-CRLH phase shifter options. Figure reproduced from [54]. (b) Example of CRLH microstrip phase shifter. Figure reproduced from [56].

## 6.1 The Via-Less CRLH Stripline Unit Cell

In collaboration with the author of [53], the via-less CRLH stripline unit cell developed was considered for use in a stripline feed network with the goal to provide even wider band phase offsets in a network that would not affect the radiation pattern due to its enclosed nature. The unit cell was tuned for the target operating band from 8 GHz to 12 GHz (10 GHz center band with 40% bandwidth). A goal of better than 10 dB return loss was set over this bandwidth, along with a maximum phase error of  $\pm 5^\circ$ .

The design focused on implementing phase shifters for  $90^\circ$  and  $180^\circ$  offsets. Through 3D EM simulation this was achieved meeting the other goal specifications using a modified version of our original via-less unit cells. The stackup was modified slightly to provide more coupling between lines. Instead of an edge coupling, broadside coupling was used. This is not ideal since the fabrication is a little more complicated (see stackup in Fig. 6.3(b) and 3D model in Fig. 6.3(a)) and the structure may become more sensitive to manufacturing tolerances. It was necessary, however, to achieve the bandwidth desired with this unit cell. Another factor to point out is that a balanced unit cell is not necessary. An actual linear region of phase progression is desired for this application, in which the slope can be matched to that of the phase offset desired. In general the linear region of a CRLH unit cell actually is away from the resonances that characterize the frequency boundaries of each mode (LH and RH). The RH region was therefore used. The control parameters are the same but the goal is different: instead of focusing in maintaining a balanced unit cell over operating frequency range, the focus was in maximizing the linear phase bandwidth of the RH region at a specific phase offset as compared to a stripline of similar length. It is interesting to note that despite the left-hand capability of the CRLH unit cell not being used directly, the effects of all circuit elements of this unit cell assist in obtaining this wider linear right-hand phase bandwidth.

Although the goal was achieved and the performance for the  $180^\circ$  case can be seen

in Figs. 6.3(c) and 6.3(d) , the overall dimensions were slightly larger than the simple Schiffman phase shifter approach in similar stripline stackup. It is interesting to note that the Schiffman design would also require the broadside coupling approach though. Since

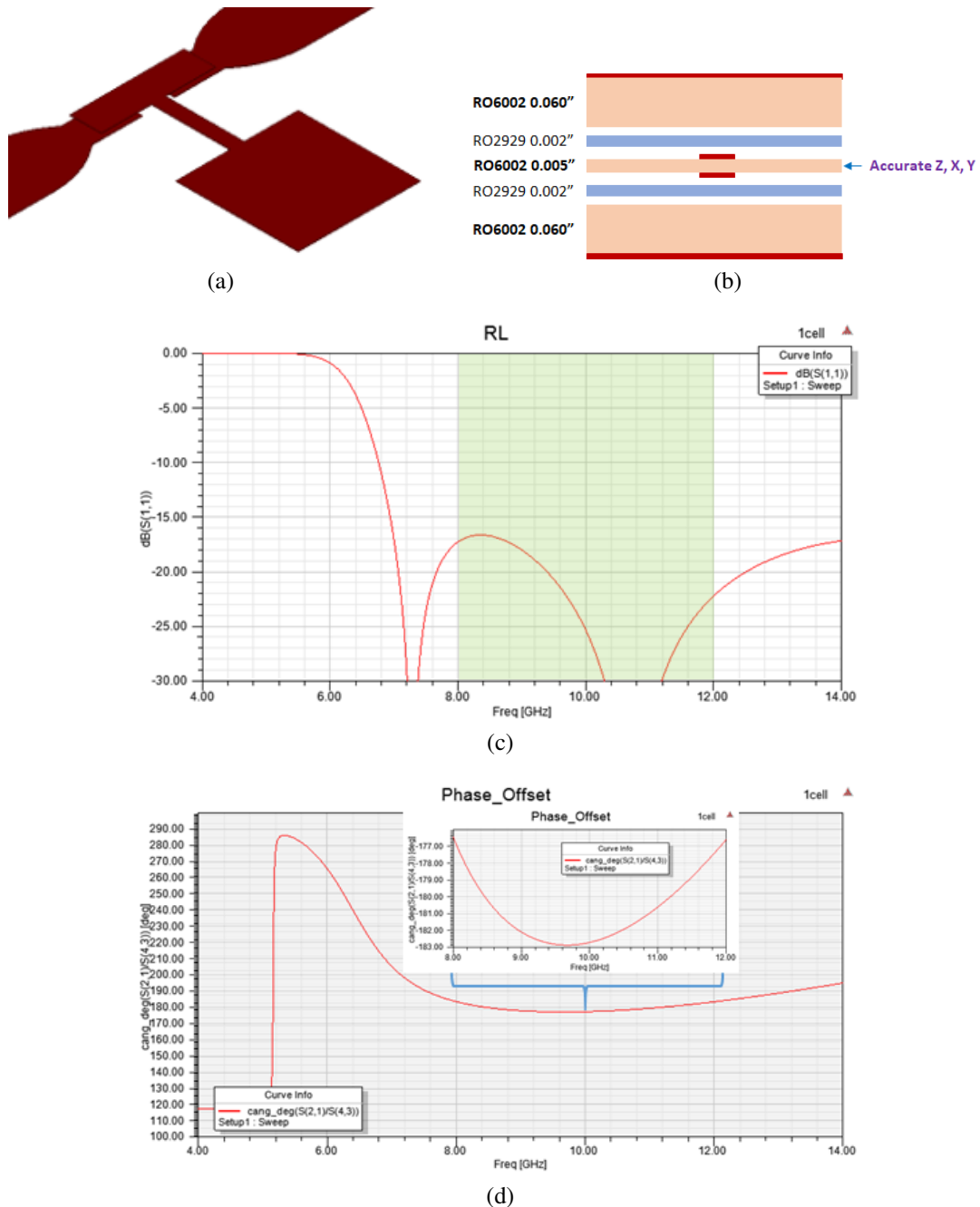


Figure 6.3: 180° Phase Shifter with via-less unit cell. (a) 3D model of the 180° Phase Shifter, (b) Stripline stackup for broadside coupling, (c) Return Loss for 180° Phase Shifter, and (d) Phase shift offset to regular stripline.

the design process for the CRLH unit cell approach is significantly more complex than that of the Schiffman, this approach appears to provide no significant advantage as is, and therefore is not recommended.

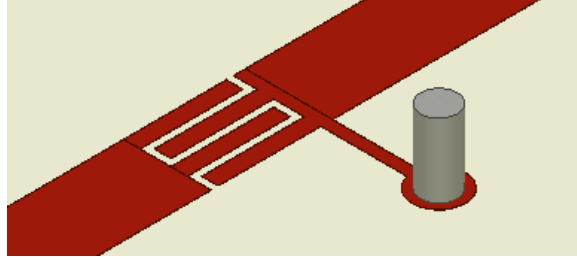
## 6.2 Traditional CRLH Stripline Unit Cell

As discussed in the previous section, the use of the via-less CRLH stripline unit cell as a phase shifting component for feed network does not offer advantages as compared to other existent phase shifting approaches. This is seen as a limitation of the via-less unit cell in particular and so the phase shifting capability of the traditional unit cell has also been explored. This has been shown to be possible in the microstrip line case [56] but has not been attempted in a stripline structure.

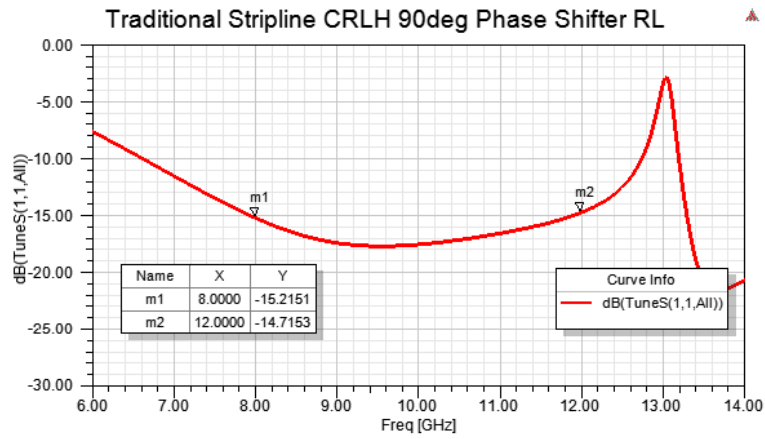
The investigation into the traditional CRLH stripline unit cell as a phase shifter has been carried out solely from a computational point of view through EM simulations of the 3D structures. The model created was chosen to have the same material set as has been used for the via-Less case, for operation in the same wide frequency bandwidth (from 8 to 12 GHz). Implementation was also focused on  $90^\circ$  and  $180^\circ$  offsets.

The tuning for wide bandwidth leads again to unbalanced unit cells, as was observed for the via-less case. The parameters used for tuning were the traditional parameters typically used for the widely adopted microstrip version, that is, the interdigital capacitor fingers quantities, width, gaps, and lengths, which adjust primarily the series capacitance of the unit cell, along with the width and length of the shorted stub that adjusts primarily its shunt inductance.

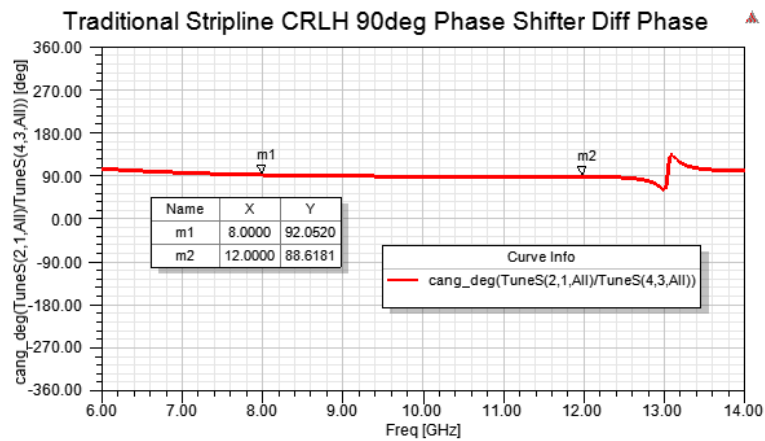
With this traditional unit cell geometry approach, the design goal was achieved with standard industry fabrication house capabilities in regards to gaps, widths and plated-through-hole via sizes. The tuned models and their respective performance parameters of interest for these two designs can be seen in Fig. 6.4 and Fig. 6.5. The two aspects in which the via-less version was lacking are for this case not an issue. First, the capacitance values



(a)



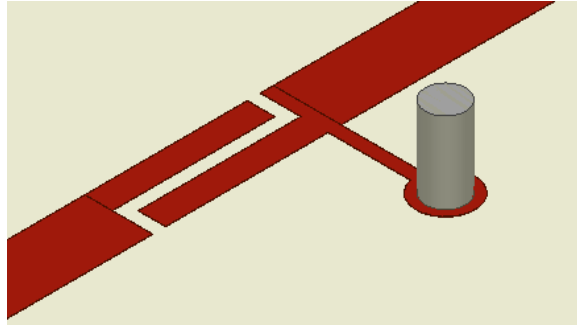
(b)



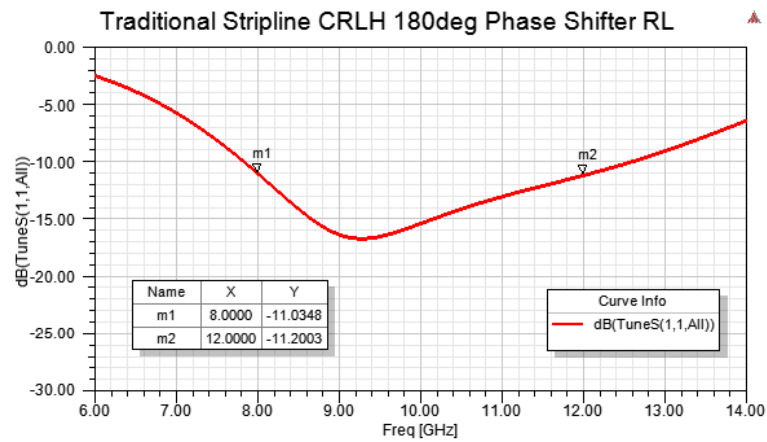
(c)

Figure 6.4:  $90^\circ$  Phase Shifter with traditional CRLH stripline unit cell. (a) 3D model. (b) Return Loss (c) Phase shift offset to regular stripline.

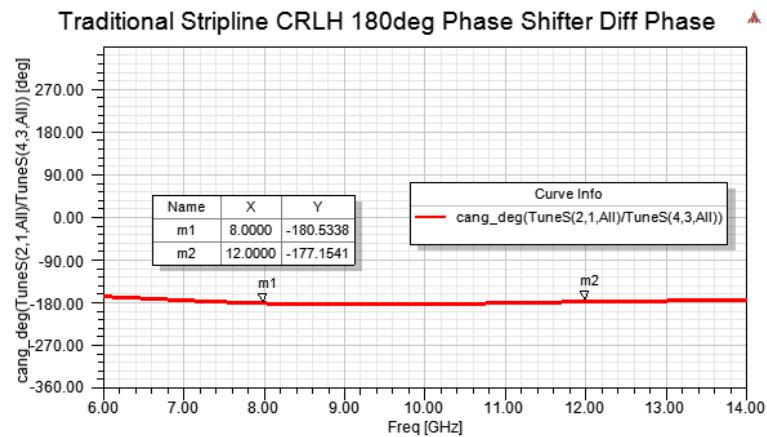
necessary under same material set is achievable without resorting to broadside coupling, which is significant because it allows a simpler stripline fabrication that even the Schiffman method did not attain. Second, the overall footprint size is slightly smaller than the typical Schiffman phase shifter approach. For the  $180^\circ$  phase shifter case, for example, the



(a)



(b)



(c)

Figure 6.5: 180° Phase Shifter with traditional CRLH stripline unit cell. (a) 3D model. (b) Return Loss (c) Phase shift offset to regular stripline.

Schiffman version measures approximately 0.2”x0.14” where as the model in Fig. 6.5(a) measures about 0.17”x0.14”.

The traditional CRLH stripline can, thus, achieve comparable wide band performance

as existent stripline phase shifters with possibly simpler fabrication, in regards to not requiring a center board due to broadside coupling, and smaller footprint size. With access to standard industry capabilities this sort of unit cell, that uses plated through holes, can be utilized to achieve wide band phase shifts throughout a stripline feed network occupying less space.

To exemplify the use of these phase shifter components, Fig. 6.6(a) shows a simple splitting feed network with four output ports consisting of three Wilkinson power dividers and transmission lines that set the phase offset such that the output ports have a  $90^\circ$  progression ( $0^\circ$ ,  $90^\circ$ ,  $180^\circ$ , and  $270^\circ$ ) at the center frequency of 10 GHz. The insertion phase graph shown in Fig. 6.6(b) depicts the absolute phase in which the offsets at 10 GHz can be observed. Fig. 6.6(c) depicts these phases using the  $0^\circ$  path as a reference by subtracting it from the insertion phase of the other ports, and further subtracting their constant phase offset value across the frequency. Fig. 6.6(c), therefore, depicts a phase error of the wide band constant offset case. This error can be significantly reduced by utilizing the traditional CRLH stripline phase shifters designed. Fig. 6.7(a) depicts the same circuit with the phase shifters, with the absolute phase and the phase error shown in Fig. 6.7(b) and Fig. 6.7(c).

### 6.3 Summary

The via-less CRLH stripline unit cell did not offer any advantage over the traditional Schiffman phase shifter for the cases explored, requiring the same stripline stackup with a center board that adds to complexity to fabrication and additional sensitivity to fabrication tolerances. It also was slightly larger. This would make it a poor choice over the traditional methods.

The traditional CRLH stripline unit cell, however, was able to obtain matching performance in regards to phase shifting and acceptable performance in terms of return loss, while occupying a smaller footprint and, more importantly, no requiring a centerboard in its fabrication. The fact that a centerboard is not required in itself presents a significant

advantage to using the traditional CRLH stripline over the Schiffman method.

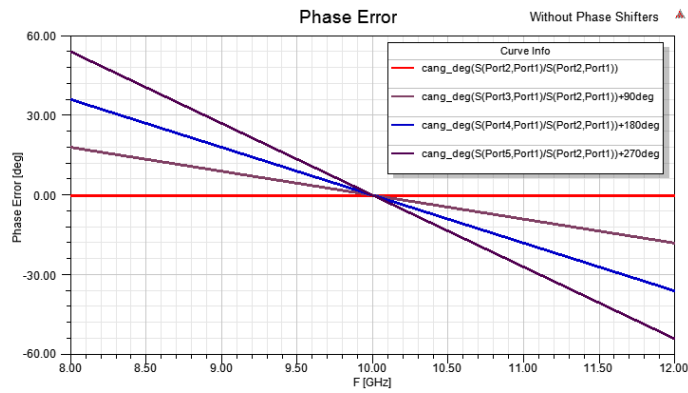
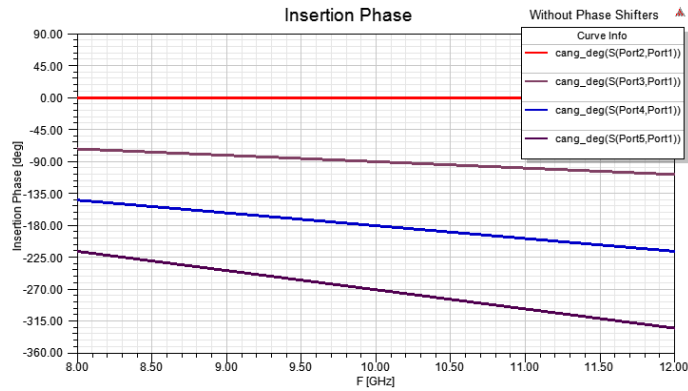
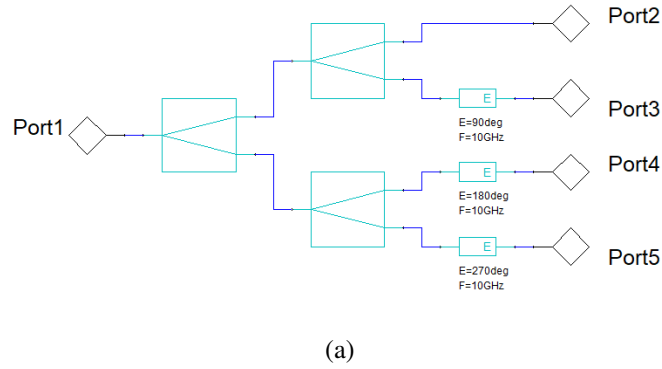
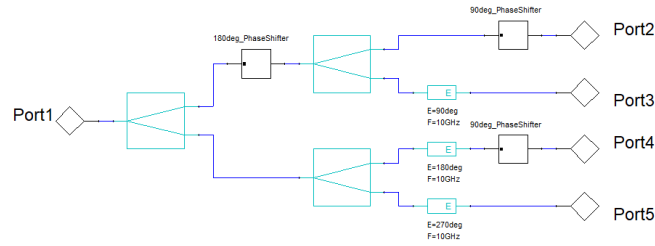
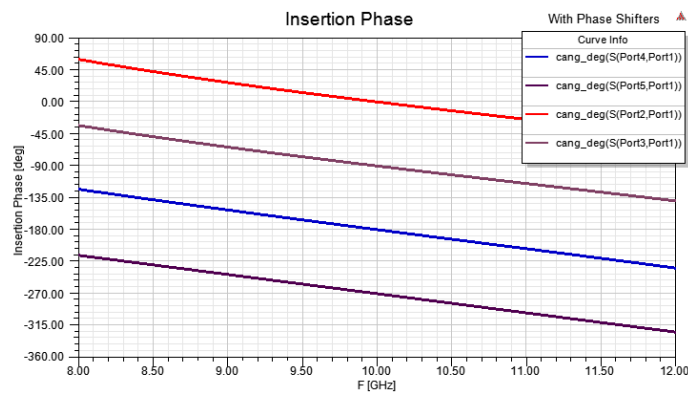


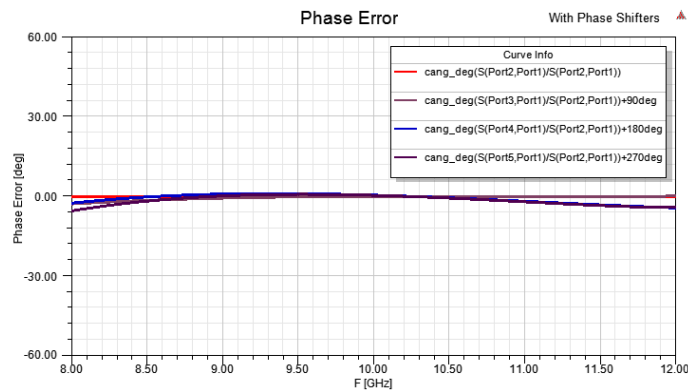
Figure 6.6: 4-Way splitting feed network with phase offsets ( $0^\circ$ ,  $90^\circ$ ,  $180^\circ$ , and  $270^\circ$ ) at 10 GHz. (a) Schematic, (b) Insertion phase, and (c) Wide band constant offset phase error.



(a)



(b)



(c)

Figure 6.7: 4-Way splitting feed network with phase offsets ( $0^\circ$ ,  $90^\circ$ ,  $180^\circ$ , and  $270^\circ$ ) at 10 GHz and with the traditional CRLH stripline phase shifters designed. (a) Schematic, (b) Insertion phase with better tracking over frequency, and (c) Wide band constant offset phase error significantly reduced.

## **CHAPTER 7**

### **METHODOLOGY**

The following is the methodology that has been followed throughout the research work for this dissertation:

#### **1. Conception**

A seeding concept of using CRLH TLs for 2D frequency scanning arrays in a raster scanning manner was introduced by one of the advisors (Prof. Choi) as possible research area of interest. A stripline version of a CRLH TL was then envisioned to protect the radiation patterns from the phase propagation feed network. The stripline structure was then also considered for use in other applications.

#### **2. Literature review**

A literature review was performed to understand the characteristics of generic CRLH TLs and general application cases. A more in depth search focused specifically on reported work regarding the use of CRLH TLs in frequency scanning array applications, and the various types of structural implementations (lumped, microstrip, etc...) of CRLH TLs that have been proposed.

#### **3. Formalization of goals and development steps**

The concept of desired contribution was formalized based on the literature review. To meet this goal, validation prototype specifications were set: complexity, frequency range, and general structural characteristics. The constitutive design steps to fully validate concept were defined: unit cells, power dividers, antenna elements, feed network, and antenna array.

#### **4. Development (Iterative Analysis)**

The synthesis part of each design step was performed by an iterative 3D Fullwave

Electromagnetic analysis (Ansys HFSS [22]) process. Iterative analysis is often the method used in microwave circuit design.

- EM eigenmode analysis was utilized for initial unit cells tuning of phase dispersion characteristics.
- Scattering parameters were extensively used in tuning of amplitude and phase of the subsections.
- Antenna array factor theory was used prior and during EM simulations to guide structural and scattering parameter goals.
- Far field EM radiation (calculated automatically by software through transformation of near-field EM radiation analysis) was used for verifying important radiating characteristics.

## 5. **Implementation** (Fabrication)

The various test boards and prototypes that were built to verify performance of design were fabricated using Syracuse University's resources, including equipment by CASE center and Prof. Matthew Maye's Lab of the Chemistry Department. A mix of routing and wet etching was used in the process. The following is a description of general steps that were necessary to build the Stripline kind of structures under study:

- AutoCAD drawings creation (for routing & wet etching)
- Wet etching
  - Cutting of patterns on Ruby Photomasks
  - Photo resist deposition using spinning device
  - Pattern exposure to UV light
  - Development
  - Etching

- Bonding of top and bottom boards of stripline, applying pressure through clamps and following recommended temperature profiles in the baking process.
- Routing of vias, cavities, and outlines
- Soldering of resistors, via rivets (barrels), and connectors

In Chapter 8 some important considerations related to some of the steps of this part of the process is provided.

#### 6. **Validation** (Measurements)

Validation of several concepts investigated was carried out through microwave measurements of test boards and prototypes. The measurements were then compared with simulated predicted performance. The measurements were primarily of scattering parameters and far field radiation patterns. The equipment utilized was available from our Microwave Lab or CASE center:

- Vector Network Analyzer (VNA) for scattering parameters
- Anechoic Chamber (including switches, rotation equipment, and VNA) for radiation measurements
- Multimeter for resistance measurements
- Camera for distance measurements (line widths and gaps)

## **CHAPTER 8**

### **MANUFACTURING CONSIDERATIONS**

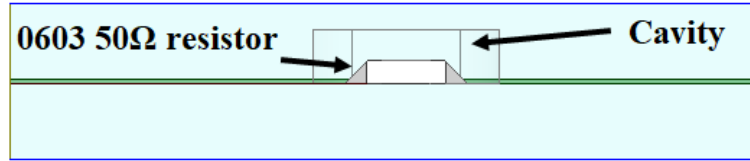
This chapter summarizes the main manufacturing issues that were overcome during the course of fabricating the various test boards and prototype throughout the research work. The information herein should be of significance to individuals fabricating their own boards either due to funding constraints or due to interest in understanding the manufacturing processes involved, which is an important factor in doing practical research.

#### **8.1 Embedding Resistors**

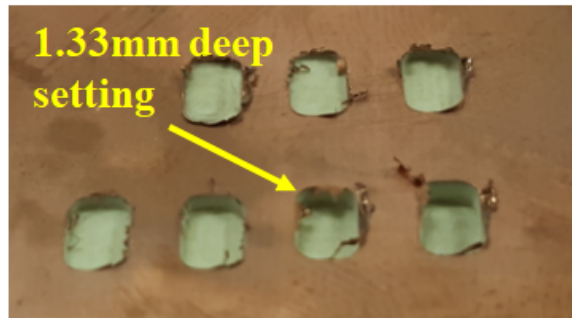
One drawback when working with stripline circuits is the reduced accessibility to the signal layer when compared to microstrip circuits. The use of surface mount components becomes challenging because the center layer is not exposed for soldering. There are several ways to address this issue with the most common being: Working around it by avoiding the use of the components, as was the case in the test board of Fig. 4.7(a) in which the isolated port of the coupler was left as an open circuit rather than terminating; Routing to a component out of the board through vias to the top layer or to the edge of the board through a connector; and Exposing the center conductor by cutting through the superstrate and then performing soldering operation through the hole after the board is built, similar to how the connectors were assembled for the prototypes in Fig. 5.8(a) and Fig. 5.11(a), among others.

Here is where fabricating a board in-house presents an advantage since by having access to the boards prior to bonding, it is possible to solder the resistors directly. This process is available in industry but not available at all fabrication houses since it requires assembly capabilities besides the regular board fabrication capability.

To avoid damaging the resistor during the bonding process, one needs to ensure there is some relief on the superstrate such that pressure during bonding will not compress the



(a)



(b)

Figure 8.1: Cavities for embedded resistors. (a) 3D Model. (b) Drill test to determine proper depth setting.

resistor. A hole in the superstrate would be possible, but ideally a cavity can be used as depicted in the model shown in Fig. 8.1(a). In order to make sure that the depth setting used when drilling would be sufficient for the resistor's safety, several drill depth settings were tested on a dummy laminate, as seen in Fig. 8.1(b). For our resistors and routing machine, the setting that yielded the best depth was 1.33 mm.

The cavities were drilled at the location of the resistors on the superstrates, as can be seen in the example superstrate in Fig. 8.2 below.

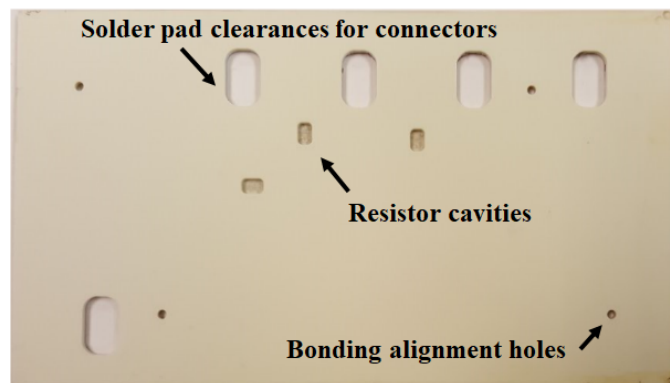


Figure 8.2: Example of cavities for resistors. Superstrate that mates with substrate in Fig. 5.6.

## 8.2 Mechanical Etching and Drilling

One useful equipment that is available to the research group is one of the milling machines by the German company LPKF [57]. It was used to perform the entire mechanical etching and drilling operations on the earliest prototype (Fig. 4.7(a)). It is a great tool for prototyping of microwave frequency test boards allowing for quick design iterations. The machine needs routine calibrations and tuning to avoid common issues associated with drilling/milling machines when used for high frequency circuits fabrication. Some issues that are worth pointing out that can prevent fabrication of good performing boards are:

- **left over burrs when drilling through metallic layers:** An example of these can be seen from the cavity drilling test (Fig. 8.1(b)) discussed in the previous section. The burrs are the pieces of metal at the edges of the cavities. In an industrial setting the drilling step is often followed by a *deburring* process. For our purposes any existing burrs were removed by *scalpel* tools.
- **uneven etching of metalization:** due primarily to difficulties in ensuring the flatness of the board on the equipment plate during the milling operation, it is difficult to find a milling depth setting that performs well over the whole board avoiding both under milling, in which case a thin layer of metalization may be left behind, and over milling, in which case a significant amount of the substrate material ends up being removed in addition to the metalization. In Fig. 4.7(a) the great open areas in which copper was removed can easily be seen along with the routing paths used. To achieve this it was necessary to perform the milling operation several times, slowly increasing the milling depth. One obvious potential consequence of under milling is the shorting of conductors that are not meant to contact each other. The main effect of over milling is observed in edge coupled lines because the strong odd mode [21] fields lie precisely in the area which can be considerably different than what was modeled. This difference is more pronounced in microstrip based coupled lines because the

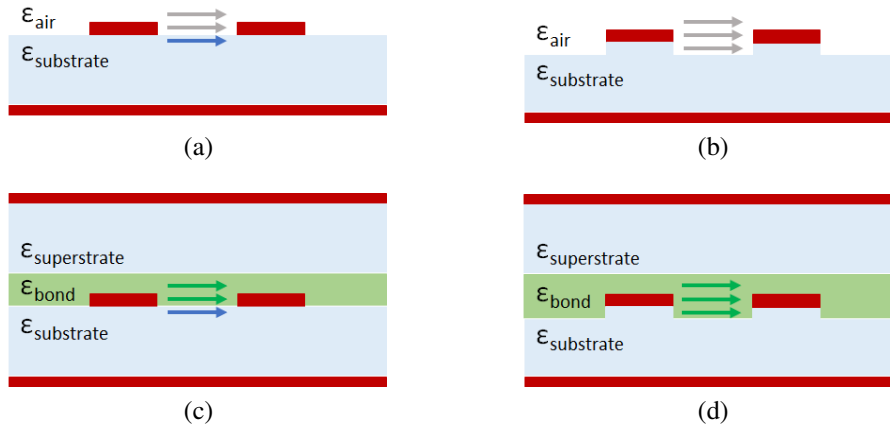


Figure 8.3: Simplified illustration of odd mode electric fields of edge coupled lines in: (a) microstrip with perfect etching (as commonly modeled). (b) microstrip with over milling. (c) stripline with perfect etching (as commonly modeled) (c) stripline with over milling.  $\epsilon_{air} < \epsilon_{substrate}$  and  $\epsilon_{bond} \approx \epsilon_{substrate} = \epsilon_{superstrate}$ .

difference in the expected permittivity in the area is between the permittivity of the substrate and that of air (see Fig. 8.3(a) and Fig. 8.3(b)). In the case of stripline technology with the use of a bonding film, the variation is smaller since the bonding film fills the void (see Fig. 8.3(c) and Fig. 8.3(d)) and its permittivity can be chosen to match as much as possible the permittivity of the substrate and superstrate. Yet, this can still be a significant issue for CRLH striplines since there is still a discrepancy in permittivity and the propagation through the line depends on the coupling values.

- **lifting of thin metalization sections:** when milling through the metalization to carve out thin lines, the *end mill* bit exerts a shear force on the metal edge that is to remain. The substrates can come with metal foils that have been attached through different methods such as electrodeposited or through adhesives. The type of metalization in the substrates used in our experiments are electrodeposited and have high *peel strength*, yet in some instances peeling of the narrow lines (see Fig. 4.1(c)) occurred during attempts at etching the pattern in 4.7(a).
- **resin melting when routing for long distances:** if the drill speed is too fast, the temperature of the bit increases significantly after routing over a distance. The high

temperature bit can melt (or *smear*) the resin in the substrate where it makes contact and when cooled it can solidify creating a bond with the base plate making it difficult to remove the part once routing is completed, but also leaving behind rough lumps on the base plate that affects the ability to keep future boards flat on the plate. Drill speed should be controlled to minimize these cases.

### 8.3 Chemical Wet Etching

The process of *photolithography* provides several benefits over the mechanical drilling method in terms of pattern accuracy. It involves transferring a pattern using ultra violet (UV) light onto a thin layer of photo resistive material on the surface of the substrate metalization using a (photo) mask [58]. Through the use of a developing solution, the exposed resistive material is dissolved, and what remains is a pattern of resistive film that was originally masked. The substrate can then be submerged into an etching solution that reacts chemically with the exposed metalization removing it, with the metalization protected by the thin resist film remaining intact. This technique is the industry standard for PCB fabrication and due the hazardous chemicals involved, requires a proper laboratory environment with safety protocols.

Chemical wet etching was utilized for all prototypes in this research work with exception of the one in Fig. 4.7(a). A laboratory in the Chemistry Department at Syracuse University was used for several steps of this process. The etching solution utilized was the Ferric Chloride ( $FeCl_3$ ) and training in handling and safety protocols were provided by the department. The main advantages to this work in using this method as opposed to the mechanical etching in the previous section is that the metalization is removed without affecting the substrate material since it does not react with the etching solution. In addition, narrower lines were also achievable without lifting off the substrate.

The amount of time in which the substrate is submerged in the etching solution, as well as the amount of movement of the etching solution, affects the ultimate line widths/gaps

of the lines. In a similar way as the milling depth in the mechanical milling case, if the etching time is too little, the solution will not remove enough copper where it needs to, and if the etching time is too long, it will continue to etch the edges of the metalization that is under the resistive film since although the top of the metalization is protected by the film, the edges will at this point be in contact with the solution. In industrial settings the whole process is performed in standard panel sizes in which ideal timings and submerging methods have been established and are tightly controlled in order to obtain line width variations of up to  $\pm 0.0005''$  for 1/2oz Copper foil thicknesses as the ones used. Typically all pattern edges in the mask are offset by a specific amount to account to a little bit of over etching expected.

For the wet etched prototypes built in this work, a process was developed to determine the line widths of key features after the initial attempts and based on these values, pattern edges offset factors were used to compensate for the expected over etching in subsequent builds. The process to measure the line widths/gaps was to first take pictures utilizing the camera in the LPKF machine since these can be taken at a constant height and naturally provide good contrast, as in the example in Fig. 8.4(a). Once the image is available it is imported into a vector based CAD tool (AutoCAD [59]) with an unknown scale and a slight rotation to align circuit feature edges with the Cartesian coordinate system of the tool. Auxiliary lines are drawn at the edges of features (see Fig. 8.4(b)) and distances

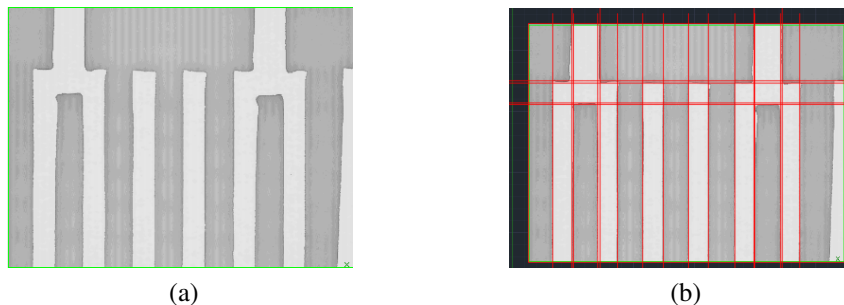


Figure 8.4: Zoomed in views of the folded via-less CRLH stripline from an iteration of the substrate in Fig. 5.6. (a) LPKF camera capture. (b) Same image with auxiliary tool lines implemented in CAD software to determine distances.

between them measured. To determine the distances of the features in the actual board, a reference measurement is made from distant features that are equally affected by etching time, such as two same sided edges on opposite sides of the image. The distance between these features on the actual board is known from the original artwork and now a scale factor can be established and applied to all other measurements.

#### 8.4 Mask Fidelity

The photo masks used to define the pattern when exposing the board with resist to UV light can also be a source of unexpected irregularities. A few different ways of generating photo masks were attempted and ultimately the ruby mask method [60] was selected. This method consists of utilizing sheets of transparent plastic with an UV blocking film with a reddish ruby color that can be cut precisely and then be peeled to form patterns for masking. One example of a ruby mask created during the research work can be seen in Fig. 8.5.

The ruby masks should be inspected carefully prior to being used. Three issues in the creation process of the ruby mask ended up affecting initial boards that were fabricated. They are:

- **displacement of small isolated sections:** after cutting the pattern on the ruby, small webs remain at corners of cuts. During the process of peeling off the undesired ruby film areas, the webs which are connected to small isolated features end up pulling

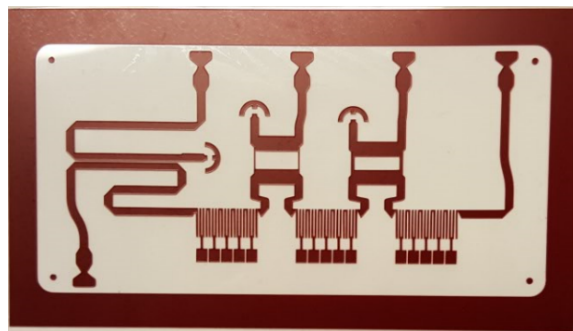


Figure 8.5: Example of ruby mask. Ruby mask for artwork of substrate in Fig. 5.6.

them too and displacing them. The solution recommended is to carefully secure the isolated features by the web locations when peeling.

- **incorrect widths of thin lines:** when cutting very thin lines and gaps it may be easily to notice significant differences between indented widths of lines, and the actual cut pattern. The solution to try to improve the widths has been to apply a scaling factor that after cutting provides the expected line and gap widths.
- **faulty CAD cutting software:** The ruby cutting pattern is programmed by a software that accepts DXF [61] file formats. Unfortunately the process of importing geometries containing arcs is faulty deforming, in various occasions, other geometry features in the region. In Fig. 8.6(a) and Fig. 8.6(b) it can be seen that segments next to arcs that were intended to be straight were converted to arcs themselves, ultimately deforming what should have been straight lines with same widths throughout. Unfortunately no straight forward solution was found in our case, so what is suggested is to replace problematic arcs with segment approximations. For example, the faulty arc in Fig. 8.6(a) was replaced by four segments as seen in Fig. 8.6(c), in which it is clear that no nearby segments were deformed.

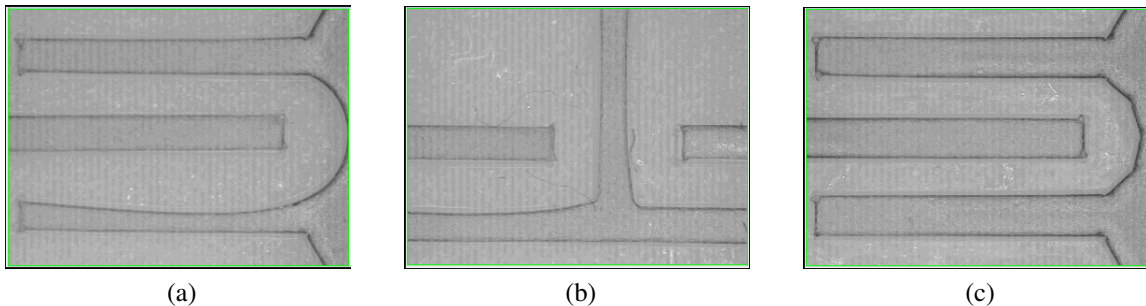


Figure 8.6: Zoomed in views of ruby masks for artwork used in same network as Fig. 5.10. (a) Example of section with arc in drawing deforming linewidths of nearby sections. (b) Another example of arc causing deformation. (c) Example of arc of same location as in (a), replaced with segment approximation not introducing deformation.

## **CHAPTER 9**

### **CONCLUSIONS**

In this work the current state of the art in regards to applications of various CRLH TLs technologies in antenna arrays has been surveyed and opportunities to contribute to the collective were identified and successfully pursued. To an extent, the main advantage in using metamaterial or CRLH structures in place of traditional ones is in the opportunity to reduce the overall circuit size for a particular application. This size reduction has been confirmed for the CRLH striplines in the application cases proposed. Tuning and performance predictions were conducted through extensive EM simulations and, in one application, an integrated antenna and feed network that conceals and protects the circuitry without a radome, has been shown possible. For the series feed network in Chapter 4, no meandering was required to demonstrate backward to forward beam scanning. For the feed network with very high phase progression discussed in Chapter 5, the phase progression circuit between the linear antenna arrays, was shown to be reduced by a factor of 5x in comparison with the traditional meandered approach in the same stackup. Finally, for the phase shifter application in Chapter 6, the CRLH stripline with traditional approach is shown capable to correct the phase slope for a  $90^\circ$  and  $180^\circ$  phase shift in a space smaller than the traditional Schiffman phase shifter approach in the same stackup.

The work performed during this research adds to the academic pool knowledge of CRLH structures by focusing on the stripline technology. The stripline technology was chosen because its shielding minimizes prospective interference from other sources, and avoids deformation of the desired radiation beams due to leaky radiation from the feed network, and striplines in general have shorter wavelengths due to higher effective permittivity when comparing to microstrips of same material set (the effective permittivity of microstrips is always reduced by the low permittivity of air). The difficult fabrication step

of attaining reliable via connections to the center conductor has been circumvented by a via-less unit cell, permitting various test boards and prototypes to be fabricated on site.

The use of novel metamaterial concepts is already being adopted in industry to reduce the cost and size of antennas with performance comparable to traditional phased array antennas. The application of the 2D frequency scanning array capable of scanning the 3D space of nearly an entire hemisphere has shown to be of significant interest in the field, having been welcomed for conference presentation and journal publication. It is the author's belief that in the near future the use of 2D frequency scanning arrays is going to be actively considered for commercial applications due to its simplicity of fabrication and operation.

Possible future research in the 2D frequency antenna array application includes further investigation into best CRLH stripline techniques to significantly increase the phase progression between linear arrays. This has the potential to drastically increase the quantity of scanning rows. Another research opportunity is in a hybrid folded via-less CRLH stripline unit cell / traditional CRLH stripline unit cell approach that has the potential to maximize the phase progression between the linear antenna arrays with the via-less cell, yet allow for reduction of the power division mechanism with the traditional cell using the CRLH TL coupler, as in Chapter 4.

# Appendices

## APPENDIX A

### MATLAB CODE: VIA-LESS CRLH TL PASSBANDS CALCULATOR

```
function vialess_crlh_passband( ze, zo, zp, zt, clen_deg, ...
plen_deg, tlen_deg, freq_ref )
%Function that plots passbands of via-less CRLH-TL
% unit cells up to 20 GHz.
%Input parameters:
% ze: Coupled lines even mode characteristic impedance
% zo: Coupled lines odd mode characteristic impedance
% zp: Characteristic impedance of open stub section
% zt: Characteristic impedance of section prior to
% open stub
% clen_deg: Electrical length of coupled lines
% plen_deg: Electrical length of open stub
% tlen_deg: Electrical length of section prior to
% open stub
% freq_ref: Reference frequency for electrical lengths

freq_list = (0.1:0.1:20)*1e9;
ctheta_list = clen_deg * pi / 180 * freq_list / freq_ref;
ptheta_list = plen_deg * pi / 180 * freq_list / freq_ref;
ttheta_list = tlen_deg * pi / 180 * freq_list / freq_ref;
throughput = zeros(size(freq_list));
lefthand = abs(2*((ze+zo)/(ze-zo))^2*(cos(ctheta_list).^2)...
-1 + (ze+zo)/(2*zt)*(zt+zp*cot(ptheta_list)).*...
```

```

        tan(ttheta_list)).*cot(ctheta_list)./...
        (zp*cot(ptheta_list)-zt.*tan(ttheta_list)).* ...
        (((ze+zo)/(ze-zo))^2*(cos(ctheta_list).^2)-1) );
righthand = 1;
throughput(lefthand <= righthand) = -10;
plot(freq_list , throughput);
end

```

## BIBLIOGRAPHY

- [1] T. K. Sarkar, R. J. Mailloux, and A. A. Oliner, *History of Wireless*. Hoboken, NJ: John Wiley & Sons, 2006.
- [2] R. M. Barrett, "Microwave printed circuits - a historical survey," *IRE Transactions on Microwave Theory and Techniques*, vol. 3, no. 2, pp. 1–9, March 1955.
- [3] K. D. Swineford and J. M. Saliba, "Stripline signal distribution system for extremely high frequency signals," U.S. Patent 6 414 573, February, 2000. [Online]. Available: <https://patents.justia.com/patent/6414573>
- [4] J. H. Choi, J. S. Sun, and T. Itoh, "Frequency-scanning phased-array feed network based on composite right/left-handed transmission lines," *IEEE Transactions on Microwave Theory and Techniques*, vol. 61, no. 8, pp. 3148–3157, Aug 2013.
- [5] M. R. M. Hashemi and T. Itoh, "Evolution of composite right/left-handed leaky-wave antennas," *Proceedings of the IEEE*, vol. 99, no. 10, pp. 1746–1754, Oct 2011.
- [6] Y. D. Dong and T. Itoh, "Composite right/left-handed substrate integrated waveguide and half-mode substrate integrated waveguide," in *2009 IEEE MTT-S International Microwave Symposium Digest*, June 2009, pp. 49–52.
- [7] S. Nishimura, H. Deguchi, and M. Tsuji, "Transmission characteristics on composite right/left-handed cylindrical waveguides constructed by the cutoff TE and TM modes," *Progress In Electromagnetics Research M*, vol. 72, pp. 89–96, 2018.
- [8] T. Yang, P.-L. Chi, and R. Xu, "Novel composite right/left-handed leaky-wave antennas based on the folded substrate-integrated-waveguide structures," *Progress in Electromagnetics Research C*, vol. 29, pp. 235 – 248, 2012.

- [9] X. Ren, K. Song, F. Zhang, and B. Hu, "Miniaturized gysel power divider based on composite right/left-handed transmission lines," *IEEE Microwave and Wireless Components Letters*, vol. 25, no. 1, pp. 22–24, Jan 2015.
- [10] L. Wang and T. J. Cui, "A novel branch-line coupler based on the composite right/left handed TL structure," in *2008 International Workshop on Metamaterials*, Nov 2008, pp. 397–399.
- [11] A. Lai, T. Itoh, and C. Caloz, "Composite right/left-handed transmission line metamaterials," *IEEE Microw. Mag.*, vol. 5, no. 3, pp. 34–50, Sep. 2004.
- [12] A. Lai, K. M. K. H. Leong, and T. Itoh, "Applications of infinite wavelength phenomenon," in *2006 European Microwave Conference*, Sep. 2006, pp. 937–939.
- [13] N. Michishita, Y. Yamada, and K. Cho, "Design of composite right/left-handed transmission line for phase shifter of multi-band base station antenna," *EPJ Appl. Metamat.*, vol. 5, p. 12, 2018. [Online]. Available: <https://doi.org/10.1051/epjam/2018009>
- [14] C. Caloz and T. Itoh, *Electromagnetic Metamaterials: Transmission Line Theory and Microwave Applications*. Wiley-IEEE Press, Nov 2005.
- [15] V. G. Veselago, "The electrodynamics of substances with simultaneously negative values of  $\epsilon$  and  $\mu$ ," *Soviet Physics Uspekhi*, vol. 10, no. 4, p. 509, 1968. [Online]. Available: <http://stacks.iop.org/0038-5670/10/i=4/a=R04>
- [16] C. Caloz and T. Itoh, "Novel microwave devices and structures based on the transmission line approach of meta-materials," in *IEEE MTT-S International Microwave Symposium Digest, 2003*, vol. 1, June 2003, pp. 195–198 vol.1.
- [17] D. K. Barton, *Modern Radar System Analysis*. Norwood, MA: Artech House, 1988.

- [18] C. A. Balanis, *Antenna Theory - Analysis and Design*, 4th ed. John Wiley & Sons, 2016.
- [19] R. C. Johnson, *Antenna Engineering Handbook*, 3rd ed. Norwood, MA: McGraw Hill, 1992.
- [20] G. L. Matthaei, L. Young, and E. M. T. Jones, *Microwave Filters Impedance-Matching Networks and Coupling Structures*. Norwood, MA: Artech House, 1980.
- [21] D. M. Pozar, *Microwave Engineering*, 3rd ed. John Wiley & Sons, 2005, pp. 371–378.
- [22] HFSS - high frequency structures simulator. Ansys. [Online]. Available: <https://www.ansys.com/products/electronics/ansys-hfss>
- [23] CST studio suite. Dassault Systemes. [Online]. Available: <https://www.cst.com/>
- [24] R. Remski, “Analysis of photonic bandgap surfaces using ansoft HFSS,” *Microwave Journal*, September 2000. [Online]. Available: <https://www.microwavejournal.com/articles/print/3044-analysis-of-photonic-bandgap-surfaces-using-ansoft-hfss>
- [25] E. Brookner, *Practical Phase Array Antenna Systems*. Artech House, 1991.
- [26] A. Sutinjo, M. Okoniewski, and R. H. Johnston, “Radiation from fast and slow traveling waves,” *IEEE Antennas Propag. Mag.*, vol. 50, no. 4, pp. 175–181, Aug 2008.
- [27] S. Paulotto, P. Baccarelli, F. Frezza, and D. R. Jackson, “Full-wave modal dispersion analysis and broadside optimization for a class of microstrip CRLH leaky-wave antennas,” *IEEE Transactions on Microwave Theory and Techniques*, vol. 56, no. 12, pp. 2826–2837, Dec 2008.
- [28] M. D. Enders and J. H. Choi, “A series feed network based on a distributed CRLH stripline for frequency scanning applications,” in *2016 IEEE MTT-S Int. Microwave Symp. (IMS)*, May 2016.

- [29] J. H. Choi, C. M. Wu, H. Lee, and T. Itoh, "Vialess composite right/left-handed stripline and its applications for broadband 3-dB and tunable couplers," in *2014 44th European Microwave Conference*, Oct 2014, pp. 315–318.
- [30] J. A. Kong, *Electromagnetic Wave Theory*. Cambridge, MA: EMW Publishing, 2005.
- [31] M. S. Mirotznik, S. Yarlagadda, R. McCauley, and P. Pa, "Broadband electromagnetic modeling of woven fabric composites," *IEEE Transactions on Microwave Theory and Techniques*, vol. 60, no. 1, pp. 158–169, Jan 2012.
- [32] J. C. Rautio, R. L. Carlson, B. J. Rautio, and S. Arvas, "Shielded dual-mode microstrip resonator measurement of uniaxial anisotropy," *IEEE Transactions on Microwave Theory and Techniques*, vol. 59, no. 3, pp. 748–754, March 2011.
- [33] C. Caloz, A. Sanada, and T. Itoh, "A novel composite right-/left-handed coupled-line directional coupler with arbitrary coupling level and broad bandwidth," *IEEE Transactions on Microwave Theory and Techniques*, vol. 52, no. 3, pp. 980–992, March 2004.
- [34] E. Brookner, "Metamaterial advances for radar and communications," in *2017 IEEE Radar Conf. (RadarConf)*, May 2017, pp. 1614–1621.
- [35] T. Geibig, A. Shoykhetbrod, A. Hommes, R. Herschel, and N. Pohl, "Compact 3D imaging radar based on fmcw driven frequency-scanning antennas," in *2016 IEEE Radar Conf. (RadarConf)*, May 2016.
- [36] S. Zhan-shan, R. Ke, C. Qiang, B. Jia-jun, and F. Yun-qi, "3D radar imaging based on frequency-scanned antenna," *IEICE Electronics Express*, vol. 14, no. 12, pp. 1–10, 2017.

- [37] W. Mayer, M. Wetzel, and W. Menzel, "A novel direct-imaging radar sensor with frequency scanned antenna," in *IEEE MTT-S Int. Microwave Symp. Dig.*, 2003, vol. 3, June 2003, pp. 1941–1944 vol.3.
- [38] Y. Alvarez-Lopez, C. Garcia-Gonzalez, C. Vazquez-Antuna, S. Ver-Hoeye, and F. L. H. Andres, "Frequency scanning based radar system," *Progress In Electromagnetics Research*, vol. 132, pp. 275–296, 2012.
- [39] A. Hommes, A. Shoykhetbrod, and N. Pohl, "A fast tracking 60 GHz radar using a frequency scanning antenna," in *2014 39th Int. Conf. Infrared, Millimeter, and Terahertz waves (IRMMW-THz)*, Sept 2014.
- [40] H. V. Nguyen, S. Abielmona, A. Rennings, and C. Caloz, "Pencil-beam full-space scanning 2D CRLH leaky-wave antenna array," in *2007 Int. Symp. Signals, Systems and Electronics*, July 2007, pp. 139–142.
- [41] M. Salarkaleji, M. Eskandari, J. C. M. Chen, and C. T. M. Wu, "Metamaterial-based microwave tomography and remote sensing using linear sampling method," in *2017 IEEE Conf. Antenna Measurements Applications (CAMA)*, Dec 2017, pp. 178–181.
- [42] M. D. Enders and J. H. Choi, in *2016 IEEE Int. Symp. Antennas and Propagation (APSURSI)*.
- [43] S. Gupta and C. Caloz, "Real-time 2-D spectral-decomposition using a leaky-wave antenna array with dispersive feeding network," in *2015 IEEE Int. Symp. Antennas and Propagation USNC/URSI National Radio Science Meeting*, July 2015, pp. 29–30.
- [44] M. Salarkaleji, M. A. Ali, and C. T. M. Wu, "Two-dimensional full-hemisphere frequency scanning array based on metamaterial leaky wave antennas and feed networks," in *2016 IEEE MTT-S Int. Microwave Symp. (IMS)*, May 2016.

- [45] M. D. Enders, J. H. Choi, and J. K. Lee, "Integrated full-hemisphere space-to-frequency mapping antenna with CRLH stripline feed network," *IEEE Trans. Microw. Theory Techn.*, vol. 66, no. 11, pp. 4765–4772, Nov 2018.
- [46] Matlab griddata function - interpolate 2-D or 3-D scattered data. Mathworks, Inc. [Online]. Available: <https://www.mathworks.com/help/matlab/ref/griddata.html>
- [47] S. T. Yang and H. Ling, "Application of a microstrip leaky wave antenna for range-azimuth tracking of humans," *IEEE Geosci. Remote Sens. Lett.*, vol. 10, no. 6, pp. 1384–1388, Nov 2013.
- [48] M. I. Skolnik, *Introduction to Radar Systems*, 2nd ed. McGraw-Hill, 1980.
- [49] E. H. Boyenval, "Pulse compression research in the united kingdom," in *Proceedings of the Eighth Symposium of the AGARD Avionics Panel*, W. T. Blackband, Ed., Royal Radar Establishment. London, U.K.: Gordon and Breach Science, September 1964, pp. 35–46.
- [50] R. H. Dicke, "Object detection system," U.S. Patent US2 624 876A, 1945. [Online]. Available: <https://patents.google.com/patent/US2624876>
- [51] K. Milne, "The combination of pulse compression with frequency scanning for three-dimensional radars," *Radio and Electronic Engineer*, vol. 28, no. 2, pp. 89–105, August 1964.
- [52] C. F. Coombs, Jr., *Printed Circuits Handbook*, 6th ed. New York, NY: McGraw Hill, 2008.
- [53] J. M. Kovitz, J. H. Choi, and Y. Rahmat-Samii, "Supporting wide-band circular polarization: CRLH networks for high-performance CP antenna arrays," *IEEE Microwave Magazine*, vol. 18, no. 5, pp. 91–104, July 2017.

- [54] M. Wei, P. Gjurovski, and R. Negra, “90° broadband asymmetrical open-short-stub phase shifter with inductance compensation,” in *2016 46th European Microwave Conference (EuMC)*, Oct 2016, pp. 979–982.
- [55] B. M. Schiffman, “A new class of broad-band microwave 90-degree phase shifters,” *IRE Transactions on Microwave Theory and Techniques*, vol. 6, no. 2, pp. 232–237, April 1958.
- [56] Y.-z. Zou, Z.-l. Lin, T. Ling, J. Yao, and S. He, “A new broadband differential phase shifter fabricated using a novel CRLH structure,” *Journal of Zhejiang University-SCIENCE A*, vol. 8, no. 10, pp. 1568–1572, Oct 2007. [Online]. Available: <https://doi.org/10.1631/jzus.2007.A1568>
- [57] LPKF - leiterplatten-kopierfrsen. Garbsen, Germany. [Online]. Available: <https://www.lpkf.com/en/>
- [58] R. C. Jaeger, “Introduction to Microelectronic Fabrication,” ser. Modular Series on Solid State Devices, G. W. Neudeck and R. F. Pierret, Eds. Upper Saddle River, NJ: Prentice Hall, 2002, vol. 5.
- [59] AutoCAD. Autodesk. [Online]. Available: <https://www.autodesk.com/products/autocad/overview>
- [60] G. E. Anner, *Planar Processing Primer*. New York, NY: Van Nostrand Reinhold, 1990.
- [61] DXF (autoCAD drawing interchange format) family, ASCII variant. Library of Congress. [Online]. Available: <https://www.loc.gov/preservation/digital/formats/fdd/fdd000446.shtml>

## VITA

Michael Douglas Enders was born September 12th, 1982 in Natal, Brazil, and currently resides in Jamesville, NY.

### Academic Degrees

2007 *Masters of Science in Electrical Engineering (Microwave Engineering)*  
Syracuse University, Syracuse, NY

2005 *Bachelors of Science in Electrical Engineering (Telecommunications)*  
Federal University of Rio Grande do Norte, Natal, Brazil.

2001 *Technician in Informatics (Electronics)*  
Federal Center of Technological Education of Rio Grande do Norte, Natal, Brazil.

### Fellowships and Awards

2006 Awarded Gerst-Hair Graduate Studies Fellowship by Anaren, Inc. and Syracuse University

2005 Awarded Winter Course Scholarship by the German Academic Exchange Service (Deutscher Akademischer Austauschdienst - DAAD)

### Publications

#### Journal Articles

J1. M. D. Enders, J. H. Choi, and J. K. Lee, "Integrated full-hemisphere space-to-frequency mapping antenna with crlh stripline feed network," *IEEE Trans. Microw. Theory Techn.*, vol. 66, pp. 4765-4772, Nov 2018.

#### Conference Presentations

C1. M. D. Enders and J. H. Choi, "A series feed network based on a distributed CRLH stripline for frequency scanning applications," in *2016 IEEE MTT-S Int. Microwave Symp. (IMS)*, May 2016.

C2. M. D. Enders and J. H. Choi, "3d space-to-microwave frequency mapping antenna," in *2016 IEEE Int. Symp. Antennas and Propagation (APSURSI)*, pp. 523-524, June 2016.

- C3. M. D. Enders, "Passive RF components design for an academic radar using Sonnet" in *28th Annual Review of Progress in Applied Computational Electromagnetics (ACES 2012)*, pp. 713-718, April 2012.

#### Workshop Presentations

- W1. M. D. Enders, "An overview of a wideband layer-to-layer transition design process.", Microwave Industry Talks session, in *IEEE Workshop on Microwave Passive Circuits and Filters*, Syracuse, NY, April, 2010.

#### **Professional Employment**

- 2018 - Now: *Sr. RF/Microwave Engineer*, Anaren, TTM Technologies company  
East Syracuse, NY
- 2016 - 2018: *Sr. RF Engineer*, JMA Wireless, Inc., Liverpool, NY
- 2015 - 2016: *Sr. RF/Microwave Engineer*, Anaren, Inc., East Syracuse, NY
- 2007 - 2015: *RF/Microwave Engineer I/II*, Anaren, Inc., East Syracuse, NY
- 2006: *RF Research Engineer - Intern*, Syracuse Research Corporation  
North Syracuse, NY

#### **Patents**

- 2015 *Stacked Microstrip Circuit with Integrated Support and Shielding Structure*  
Co-Inventor, (Patent Number: US9178257 B2)

#### **Professional Membership**

- 2005 - Now: *IEEE (Institute of Electrical and Electronics Engineers) Member*

#### **Volunteer Work**

- 2011 - Now: *Secretary of the Syracuse IEEE APS/MTT/EMC Joint Chapter*